Inter-void shearing effect on damage evolution under plane strain deformation in high-strength aluminum alloy sheet

Jinwoo Lee[1], Hyuk Jong Bong[2#], Jinjin Ha[3], Daeyong Kim[4*]

[1]School of Mechanical Engineering, University of Ulsan, Ulsan, 44610, Republic of Korea

[2]Department of Materials Processing, Korea Institute of Materials Science, Changwon, 51508, Republic of Korea

[3]Department of Mechanical Engineering, University of New Hampshire, Durham, NH 03824, USA

[4]Department of Intelligent Mobility, Chonnam National University, Gwangju, 61186, Republic of Korea

[#]Corresponding author (Hyuk Jong Bong)

Email address: hjbong@kims.re.kr; Tel.: +82 55 280 3560

*Co-corresponding author (Daeyong Kim)

Email address: daeyong.kim@jnu.ac.kr; Tel.: +82 62 530 4228

Abstract

In this study, the ductile damage responses of high-strength 7000 series aluminum alloy (AA), AA 7075-T6 sheet samples, subjected to the plane strain deformation mode were investigated using finite element (FE) simulations. In the experiments, uniaxial tension (UT) and plane strain tension (PST) tests were conducted to characterize the plasticity and ductile damage behavior of the AA 7075-T6 sheet samples. The limiting dome height (LDH) and V-die air bending tests were conducted to evaluate the ductility of the material subjected to plastic deformation and friction between the tools, and the corresponding fractured samples were qualitatively analyzed in terms of dimples using fractography. FE simulations were performed to predict the ductility of the AA 7075-T6 sheet samples under plane strain deformation using an enhanced Gurson−Tvergaard−Needleman (GTN) model, namely the GTN-shear model. The model was improved by adding the shear dimple effect to the original GTN model. The predicted results in terms of the load–displacement curves and displacements at the onset of failure were in good agreement with experimental data from the aforementioned tests.

Furthermore, virtual roll forming simulations were conducted using the GTN-shear model to determine the effect of the prediction on ductile behavior for industrial applications.

Keywords

Aluminum alloys; Ductility; Plane strain deformation; Damage model; Finite element.

1. Introduction

High-strength aluminum alloys (AA), particularly T6 aged aluminum alloy 7075 (AA 7075-T6), have attracted significant attention in the automotive industry in recent years owing to their strength-to-weight ratio and corrosion resistance [1], which offer important economic benefits such as reduction of CO_2 emissions and fuel consumption. Because of the Guinier–Preston (GP) zone and η precipitates, conventional T6 tempered AA 7075 sheets exhibit high strength, and the precipitation of the second phase of AA 7075-T6 affects the microstructure and damage behavior during plastic loading [2–4]. However, the major drawback of AA 7075-T6 sheets is their limited formability and larger springback at room temperature [5], which requires the use of a forming technology, such as heat-assisted forming technology, to improve the ductility of the sheets [6,7]. Heat-assisted forming technology, such as hot forming [8], warm forming [9], and W-temper forming processes [10], can improve the ductility of AA 7075-T6 sheets to produce manufactured parts; however, obstacles, such as high energy consumption to increase the temperature and low productivity, still exist [11]. Therefore, it is necessary to develop an alternative approach at room temperature.

It has been reported that roll forming technology, which is one of the candidates for room-temperature forming process, is suitable for overcoming the poor formability of high-strength materials [12]. Lee et al. [13] implemented a roll forming process for manufacturing automotive bumper beams using AA 7075-T6, and Suckow et al. [14] investigated the roll forming of high-strength AA 7075 materials under various heat treatment conditions. Roll forming technology is a bending process with a rotating tool motion to produce the desired shape [14]. In the process, sheet metals are incrementally bent into the final product, passing

through the forming roll station. As a result, plane strain bending is the major deformation mode in the roll forming process. The bending fracture limit under plane strain deformation in the roll forming process is an important material parameter [15]. Andersen et al. [16] highlighted the difference in the ductile fracture behavior of thin metals in plane strain tension and plane strain bending. Deole et al. [12] demonstrated that the V-bend test can yield an accurate fracture strain limit during a roll forming process. In addition, the study in Lundberg and Melander [17] revealed that a higher bendability of sheet metals is obtained with a smaller radius of roll forming than simple air-bending operations under plane strain deformation. Therefore, it is useful to examine the plane strain deformation of AA 7075-T6 sheet samples to prevent shape defects in the roll forming process.

In terms of numerical modeling of the ductile fracture behavior of sheet metals, ductile fracture criteria have been extensively studied in recent years to determine the material failure behavior after necking under a wide range of loading conditions [18,19]. Ductile fracture models can be categorized into two main types, namely uncoupled and coupled fracture criteria. The uncoupled fracture model can predict ductile damage in an explicit frame without coupling the constitutive equations for plastic deformation [20–22], which benefits from its simple mathematical form for fracture description and relatively simple calibration procedure with fewer experiments. Initially, a fracture model was developed based on stress triaxiality [23]. Later, Bao and Werizbicki [24,25] experimentally found that models that are based on stress triaxiality cannot accurately capture material failure in a wide range of loading conditions, and the modified Mohr–Coulomb (MMC) model was proposed based on stress triaxiality and Lode angle [26,27]. In addition, the MMC model has been extensively applied to various high-strength materials to predict crack initiation during plastic deformation [28–31].

In contrast, coupled ductile fracture models integrate ductile damage into constitutive equations for plasticity to characterize material degradation, and have been widely used in the field of sheet metal forming [32–34]. Gurson [35] modeled material degradation based on spherical voids controlled by void growth in a frame of the continuum approach, and the model itself is known to be one of the most significant physics-based models. The original model was extended to elucidate the ductile damage behavior of porous metals. Chu and Needleman [36] added void nucleation factors to the void volume fraction, and Tvergaard and Needleman [37,38] accounted for the void coalescence effect by introducing the effective porosity concept.

The abovementioned improvements in the Gurson model resulted in the Gurson–Tvergaard–Needleman (GTN) model. Numerous studies have reported that the current GTN model is beneficial for reproducing the material failure of polycrystalline metals for high-stress triaxiality [39–45]. However, the current form of the GTN model yields less accurate prediction of material failure under low-stress triaxiality conditions [46–48]. Several studies have been conducted to improve the predictive performance of the GTN model for low-stress triaxiality by introducing additional state variables for the shearing effect [49–53] and arbitrary elliptical voids in ductile metals [54–60]. A micromechanics-based shear-modified Gurson model was successfully applied to large-scale metal structures for ductile damage prediction [61]. Jeong et al. [62] proposed a modified GTN model using a multiscale finite element (FE) approach to predict the ductile fracture behavior of aluminum alloys with precipitates embedded in an aluminum matrix. In addition, Nielsen and Tvergaard [52,63] found that the shear-modified Gurson model [49] could affect the growth of fracture in the moderate stress triaxiality range, such as plane strain deformation.

To the best of the authors' knowledge, Hong et al [64] have recently evaluated the bendability of the high-strength aluminum alloy sheets but only a plasticity model was applied to predict the bending property of the high-strength aluminum alloy sheets. Thus, the objective of this study is to propose FE simulation methods with the enhanced damage model to capture the ductile damage behavior of AA 7075-T6 sheet samples under plane strain deformation at room temperature. The rest of this paper is organized as follows: Section 2 presents the experimental procedure for the tensile, limiting dome height (LDH), and V-die bending tests. The major deformation modes for the experiments were uniaxial tension and plane strain tension deformations. In Section 3, the material models for characterizing the plasticity and ductile damage properties are presented. The non-quadratic isotropic plastic yielding model and enhanced Gurson-type damage model were used in the numerical simulation. Furthermore, the micromechanics-based damage model, the Gurson-type model, was used in the numerical simulations. A comparison of the experimental and numerical results was performed, as presented in Section 4. Virtual roll forming simulations were performed using the proposed material model to determine the onset of the material failure during the forming process. The main conclusions drawn based on the findings of this study are summarized in Section 5.

2. Experimental procedure

2.1. Material

Aluminum alloy (AA) 7075-T6 sheets with a thickness of 2.54 mm (0.1 in) produced by AMAG company were used in this study; T6 temper has superior strength and corrosion resistance ratings [65]. The chemical compositions of the material are listed in Table 1. The microstructure of the as-received material obtained using optical microscopy (OM) is shown in Figure 1. The etchant used in the microscopic examination was Keller's reagent [66]. The OM image of the as-received material reveals the presence of randomly distributed inclusions (black dots in the figure) and an average grain size of approximately 80 μm.

Table 1. Chemical composition of AA 7075-T6 sheets (unit: wt%)

Si	Fe	Cu	Mn	Mg	Cr	Zn	Ti	Al
≤0.4	≤0.5	1.2−2.0	≤ 0.3	2.1−2.9	0.18 −0.28	5.1−6.1	≤ 0.2	Bal.

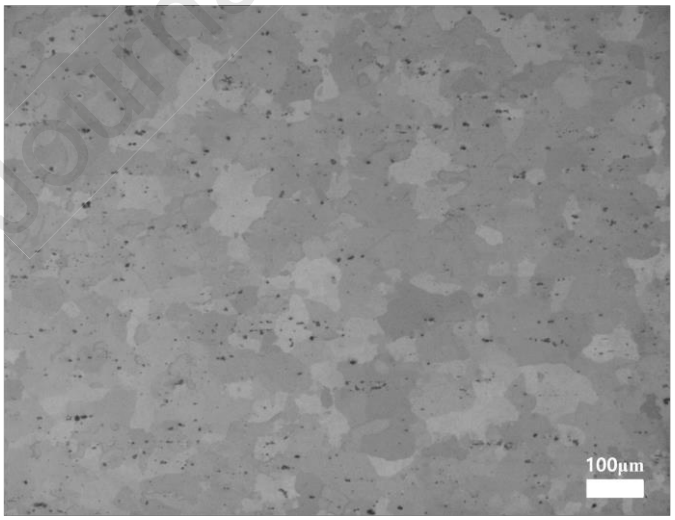

Figure 1: Optical microscopy image of AA 7075-T6 sheets. Black dots in the figure indicate inclusions.

2.2. Tensile tests for uniaxial and plane strain deformation modes

Tension-based tests were conducted in uniaxial and plane strain deformation modes using a universal testing machine (UTM). Figure 2 (a) shows the test machine with a load cell capable of measuring loads of up to 98 kN. Figure 2 (b) shows the notched specimen geometry with a gauge length of 12 mm for the plane strain tension (PST) tests. ASTM-E8 standard specimen samples were used for the uniaxial tension (UT) tests. The tensile axis was aligned with the rolling direction (RD), and a constant cross-head speed of 0.05 mm/s was applied, corresponding to a quasi-static loading condition. The load signal during testing was measured using the load cell, and the displacement of the gauge length and the strain distribution on the surface were tracked using the ARAMIS 3D digital image correlation (DIC) system, as shown in Figure 2 (a). The images were captured at the rate of 4 fps. A minimum of three tests were conducted to confirm the repeatability of the tests.

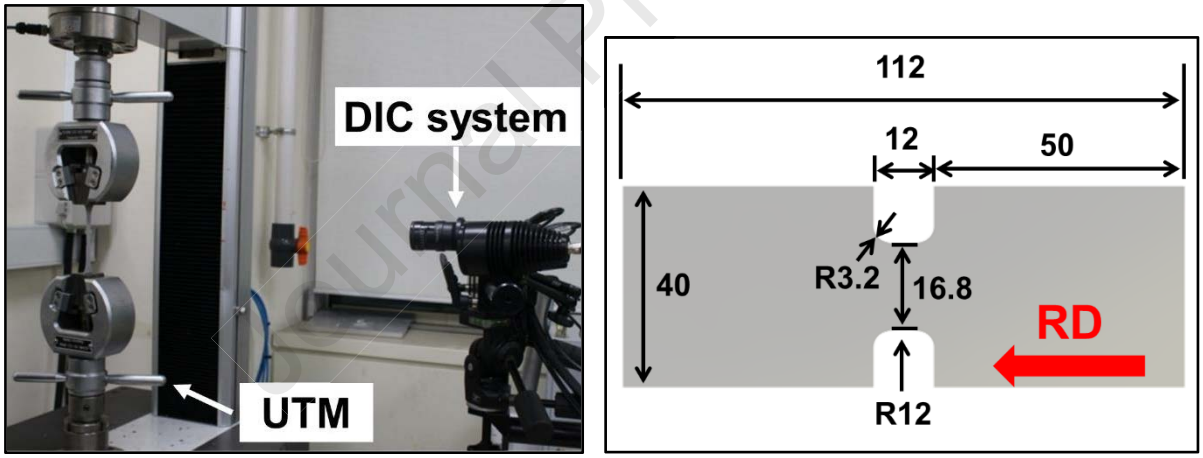

(a) (b)

Figure 2: (a) Universal testing machine with a DIC measurement system, and (b) specimen shape and dimension for plane strain deformation (unit: mm) [34].

2.3. Limiting dome height tests for plane strain deformation

Limiting dome height (LDH) tests were conducted for AA 7075-T6 sheets in accordance with the ISO 12004-2 standard using a universal sheet metal test machine (ERICHSEN GmbH, model 142-40). Figure 3 (a) depicts the detailed tooling dimension for the LDH tests consisting

of a die, punch, and holder. A hemispherical punch with a radius of 50 mm was used, and the punch speed and holding force were 0.05 mm/s and 200 kN, respectively. The punch load and its moving stroke were recorded during the test. A Teflon sheet with a thickness of 0.1 mm and solid grease lubricant were employed to minimize the effect of friction between the punch and specimen.

The specimen geometry in the LDH tests is shown in Figure 3 (b), which illustrates the plane strain deformation mode during the test [48]. The deformation path of the specimens was confirmed from previous experimental works [67,68]. The main loading direction of the specimens was along the RD. Similar to the tensile tests, a stochastic pattern was applied to the surfaces of the specimens using white and black permanent markers, and at least three tests were conducted to verify the repeatability of the LDH tests. The strain distributions on the surfaces of the samples during the test were obtained using an ARAMIS 3D DIC system with two in-situ monitoring cameras. The images were captured at 10 fps.

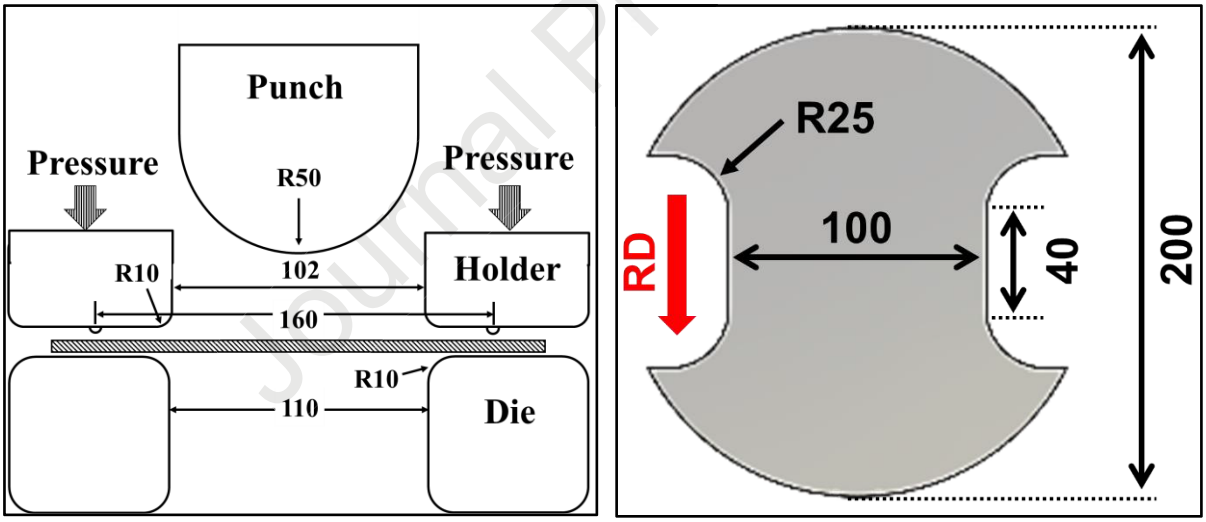

(a) (b)

Figure 3: (a) Schematic diagram of the limiting dome height tests, and (b) specimen for the plane strain deformation mode (unit: mm) [48].

2.4. V-bending tests

Figure 4 (a) shows the experimental setup for the V-bending test for the plane strain bending deformation. The V-die bending tests were conducted using a UTM with a load capacity of 98

kN; the dimensions of the tools are shown in Figure 4 (b). The moving speed of the punch was set to 0.1 mm/s for all the tests to maintain a quasi-static condition. The punch load was measured using a load cell, and the punch stroke was implemented using a laser extensometer by attaching a reflective laser tape to the V-die bending tools. The punch was moved up to a vertical displacement of 40 mm. The bending strain was varied using two different radii of the punch, that is, 1 mm and 5 mm. A rectangular specimen with dimensions of 200 mm × 60 mm (RD × TD) was used.

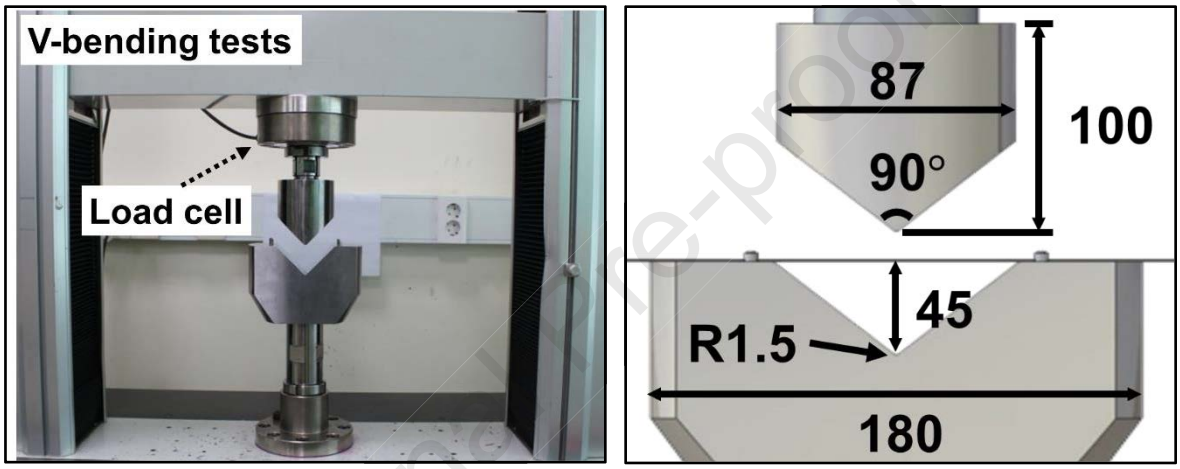

(a) (b)

Figure 4: Experimental setup used for the V-bending tests: (a) test machine and incorporated tools and (b) specific dimensions of the tools [69,70]

3. Simulation procedure

3.1. Material modeling

In this study, the plastic yielding property of AA 7075-T6 sheets was reproduced under multi-axial loading conditions using the Hershey–Hosford nonquadratic isotropic criterion [71,72]. The Hershey–Hosford criterion is mathematically formulated as

$$\Phi_1(s_1, s_2, s_3) = |s_1 - s_2|^m + |s_1 - s_2|^m + |s_1 - s_2|^m = 2(\bar{\sigma}_H)^m, \quad (1)$$

where $\bar{\sigma}_H$ is the effective stress from the Hershey–Hosford criterion, s_i (i = 1–3) is the principal value of the deviatoric stress tensor $\mathbf{s}$, and the exponent m of the criterion determines the sharpness of the yield locus. The exponent m is determined by the crystal structure of the metal; for instance, 6 for body-centered cubic (BCC) and 8 for face-centered cubic (FCC). Therefore, m = 8 was used in this study for the AA 7075-T6 material. Note that the exponent m in the Hershey–Hosford model significantly affects the plane strain deformation behavior [29].

The Swift hardening model, which considers isotropic hardening, was used to reproduce the flow stress behavior as follows [73,74]:

$$\sigma_{Iso}(\bar{\varepsilon}) = K \cdot (\varepsilon_0 + \bar{\varepsilon})^n, \quad (2)$$

where K, ε_0, and n are the material coefficients to be fitted using experimental results from uniaxial tension and $\bar{\varepsilon}$ is the effective strain.

In this study, a Gurson-type porous model based on a coupled concept for plasticity damage was utilized to simulate the ductile damage behavior of AA7075-T6 sheets. Gurson [35] initially proposed a porous material model to reproduce the void nucleation and growth process during plastic deformation. Tvergaard and Needleman [37] later modified the Gurson model to reflect the mechanism of void coalescence during inelastic deformation. The Gurson-type model assumes that a porous material consists of spherical voids surrounded by a material matrix, and the damage property is quantified using a void volume fraction. The mathematical expression for the Gurson-type porous plasticity model, that is, the GTN model, is as follows:

$$\Phi(\boldsymbol{\sigma}) = \overbrace{\left(\frac{\bar{\sigma}_{\mathrm{H}}}{\sigma_{\mathrm{Iso}}}\right)^2 - 1}^{\text{Plasticity factor}} + \underbrace{2q_1 f_* \cosh\left(q_2 \frac{3p}{2\sigma_{\mathrm{IH}}}\right) - q_3 f_*^2}_{\text{Cavities factor}} = 0\,, \tag{3}$$

where $\bar{\sigma}_{\mathrm{H}}$ is the effective stress from the Hershey–Hosford criterion, σ_{Iso} is the flow stress of the fully dense matrix material defined in Eq. (2), p is the hydrostatic pressure or negative mean stress, f_* quantifies the loss of the material stiffness during plastic deformation expressed by the total void volume fraction f, and q_1, q_2, and q_3 are material constants. The recommended values of the material constants for metallic materials in the Gurson model are $q_1 = 1.0 - 1.5$, $q_2 = 1.0$, and $q_3 = (q_1)^2$ [37]. The function f_* is expressed as

$$f_* = \begin{cases} f & f \le f_a \\ f_a + m \cdot (f - f_a) & f_a \le f \le f_b, \\ f_f & f_b \le f \end{cases} \tag{4}$$

$$m = \frac{f_f - f_a}{f_b - f_a}, \tag{5}$$

$$f_f = \frac{q_1 + \sqrt{q_1^2 - q_3}}{q_3}. \tag{6}$$

where f_a and f_b are the values of the void volume fraction at the critical point and at the onset of material failure, respectively, and f_f determines the function value when a complete loss of stiffness occurs in the material.

The total void volume fraction in the GTN model is defined as

$$f = f_{\mathrm{nucl}} + f_{\mathrm{g}}\,, \tag{7}$$

where f_{nucl} and f_{g} are the void volume fractions as a result of a new void nucleation and void growth, respectively.

The change in the void volume due to the newly nucleated void is expressed as follows:

$$df_{\mathrm{nucl}} = A \cdot (d\bar{\varepsilon}_{\mathrm{m}}) \tag{8}$$

$$A = \frac{f_N}{S_N\sqrt{2\pi}} e^{\left[-\frac{1}{2}\left(\frac{\bar{\varepsilon}_m - \varepsilon_N}{S_N}\right)^2\right]}, \quad (9)$$

where $\bar{\varepsilon}_m$ is the effective strain in the matrix, $d\bar{\varepsilon}_m$ is the incremental form of the effective strain, f_N is the new void volume fraction from nucleation, ε_N is the average value of the normal distribution of the nucleation strain, and S_N is the standard deviation of the Gaussian distribution. The strain-controlled nucleation rule and Gaussian distribution functions are associated with newly nucleated voids.

The change in the incremental void volume due to void growth during inelastic deformation is formulated as follows:

$$df_g = (1-f)d\boldsymbol{\varepsilon}_p : \mathbf{I}, \quad (10)$$

where $d\boldsymbol{\varepsilon}_p$ is the plastic strain increment tensor for the matrix material, $\mathbf{I}$ is the second-order identity tensor, and the symbol "**:**" denotes the double dot product of two tensors, which results in a volumetric strain increment.

Although the GTN model can achieve high performance in the prediction of the damage behavior at high stress triaxiality, various studies have revealed that the GTN model could be less accurate at low stress triaxiality [49,50,75,76]. To improve the model in this study, an additional term was included in the void volume fraction increment for shear df_s as follows based on Nahshon and Hutchinson [49]:

$$df_s = k_w \cdot f \cdot \omega(\theta) \cdot \frac{\mathbf{s} : d\boldsymbol{\varepsilon}_p}{\bar{\sigma}}, \quad (11)$$

where k_w is the material constant, $\mathbf{s}$ is the deviatoric stress tensor, and $\omega(\theta)$ is a function of the Lode angle θ defined as

$$\omega(\theta) = 1 - (\cos 3\theta)^2 \text{ and } \cos 3\theta = \frac{3\sqrt{3}J_3}{2J_2\sqrt{J_2}}, \quad (12)$$

where J_2 and J_3 are the second and third invariants of the deviatoric stress tensor, respectively. Note that the value of the Lode angle function $\omega(\theta)$ is zero when a uniaxial

stress state is applied, and it becomes unity and zero for the plane strain tension and balanced biaxial tension stress states, respectively.

Then, the evolution law of the total void volume fraction increment can be defined as

$$df = df_{\text{nucl}} + df_{\text{g}} + df_{\text{s}} . \tag{13}$$

Note that the model considered in this study is known as the "GTN-shear" model.

3.2. Finite element modeling

FE modeling was performed using a commercial FE ABAQUS/Explicit solver [77] to evaluate the plastic deformation and ductile damage behaviors of AA 7075-T6 sheets. And the proposed GTN-shear model was implemented via user-defined material subroutine as described in Appendix A. The FE simulations for the specimens were constructed using a 3D solid element type with an eight-node and reduced integration point (C3D8R). Figure 5 (a) and (b) show the FE models of the specimens for the two tensile tests, namely, uniaxial and plane strain tensions. A fine mesh was designed in the gauge length area with an element size of 0.1 × 0.1 × 0.254 mm^3 (length × width × thickness), whereas a coarse mesh with an element size of 1.0 × 1.0 × 0.254 mm^3 was used for the gripping region after the mesh size sensitivity tests [78]. In order to reduce the computation time, grip region in experiments were removed in the simulations, and the simulations were performed under the same boundary conditions as those used in the experiments. The load and displacement data in the gauge length area were obtained from simulations and compared with experimental data.

Figure 5 (c) shows the 3D model of the LDH tests for plane strain deformation. It consists of a punch, die, and a sheet sample. For computational efficiency, the holder system was omitted, the degrees of freedom of the sheet sample along the bead line (i.e., the outer edge) were fully constrained, and only a quarter model of the sheet sample was used considering the symmetric condition. The tools were modeled as an analytical rigid body, and a 3D solid element (C3D8R) was used for the sheet samples. The average mesh size was 1.0 × 1.0 × 0.508 mm^3 (RD × TD × thickness) and a refined mesh size of 0.3 × 0.3 × 0.508 mm^3 was used in the contact area with the punch [79,80]. A friction coefficient of 0.02 was set between the sheet sample and the tools [81].

Figure 5 (d) shows the FE model for the V-die bending test comprising a die, punch, and sheet sample. Because plane strain deformation occurs during the test, a 4-node plane strain element type with reduced integration (CPE4R) was used to reduce the computation time. The average mesh size in the contact area with the punch was set to 0.05 × 0.05 mm^2 (RD × thickness). The tools were designed as a rigid analytical body. The corresponding boundary conditions are illustrated in the figure, and a friction coefficient of 0.15 was used between the tools and the sheet sample [82]. It is worth noting that the friction coefficients for the LDH and V-die bending tests are referred to literatures. The effect of the friction coefficient on the ductility prediction is necessarily investigated as shown in Appendix B.

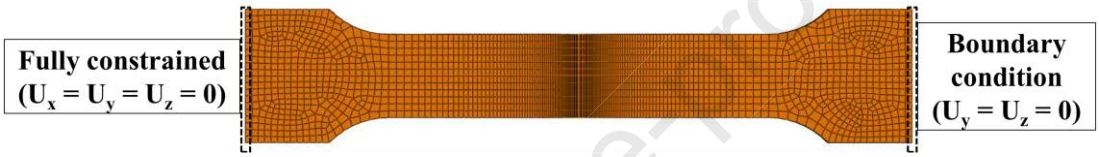

(a)

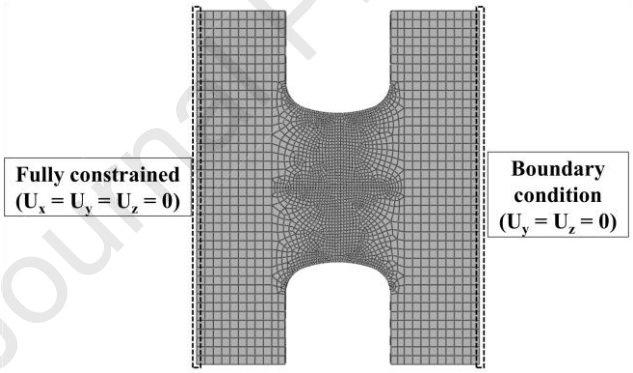

(b)

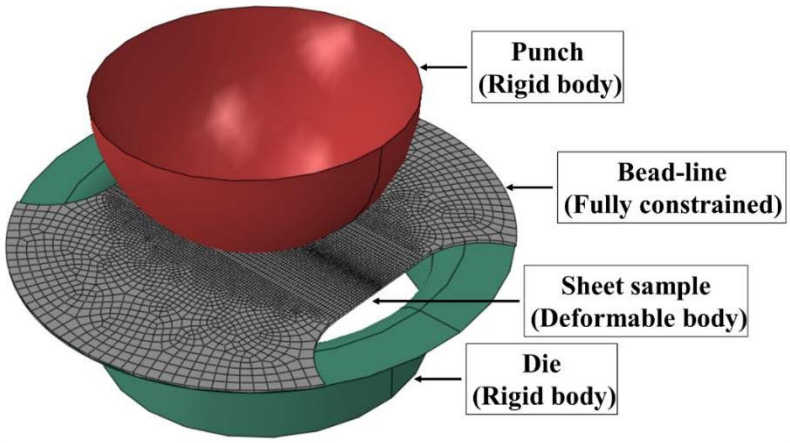

(c)

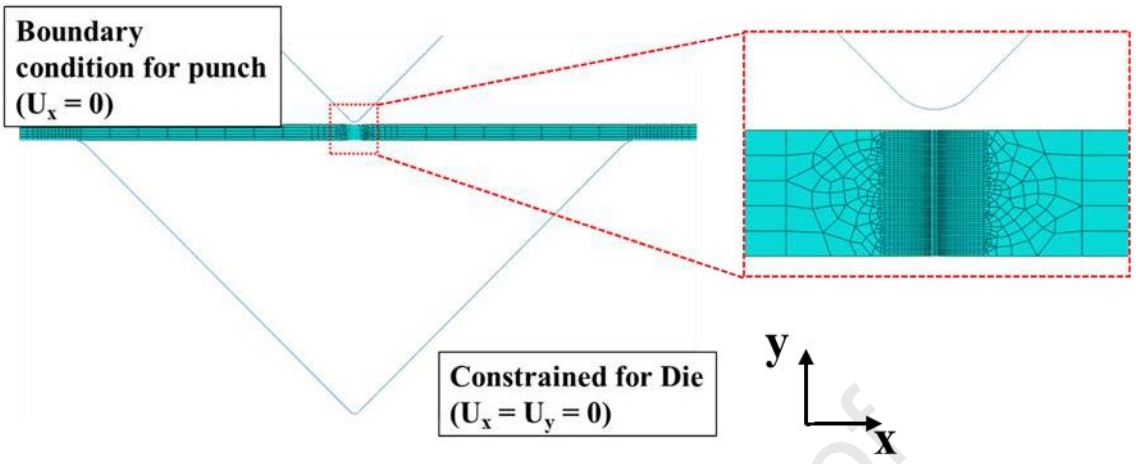

(d)

Figure 5: Finite element models for the (a) uniaxial tensile specimen, (b) plane strain tension specimen, (c) limiting dome height tests, and (d) V-die bending tests [34].

The linear isotropic elasticity law for AA 7075-T6 sheets was applied with a constant Young's modulus of 72 GPa, Poisson's ratio of 0.33, and density of 2.7 g/cm^3. To improve computation time efficiency, the mass scaling factor was carefully selected to ensure quasi-static analyses in the simulations. Therefore, the amount of kinetic energy is negligible compared with that of the internal energy.

Note that when the failure condition of the GTN-shear model is satisfied for all the integration points in the FE model, the corresponding element is removed in the FE model.

4. Results and discussions

4.1. Tensile tests: uniaxial and plane strain tension deformation

The material parameters of the GTN-type models for reproducing the ductile damage behavior from void nucleation–growth–coalescence were calibrated using experimental data from the UT test. A series of FE simulations were performed to determine the best fitting parameters of the GTN-type damage models for the load–displacement curve, where the displacement was obtained using an extensometer of a specific initial length or from engineering stress–strain curves. The parameters were calibrated in three steps, as illustrated in Figure 6. First, the parameters for the strain hardening and plastic yielding models can be determined based on the assumptions of zero initial void volume fraction and negligible increase during uniform deformation, that is, by the displacement d_1 at the maximum force (in Figure 6) [83]. Second, the parameters related to void nucleation and growth were determined between the displacements d_1 and d_2, where the displacement d_2 is close to the drastic load decrease leading to fracture. It should be noted that the displacement d_2 could be possibly detemined by calulating the second derivative of the load–displacment curve. The displacement d_2 could be defined as the displacement value corresponding to the minimum of the second derivative of the curve.

The inverse identification of the material parameters in the frist and second steps was conducted by the opimization algorithm [84–86]. A error function $\Gamma(\boldsymbol{A})$ is defined by the least square as in Eq. (14), and starting from the initial guess of the material constants $\boldsymbol{A}_0$. The error function is minimized with a Levenberg–Marquardt algorithm as follows:

$$\Gamma(\boldsymbol{A}) = \sum_{i=1}^{N} \Gamma_i(\boldsymbol{A}) \tag{14}$$

$$\text{with } \Gamma_i(\boldsymbol{A}) = \frac{1}{N_i}\sum_{i=1}^{N}(F(\boldsymbol{A}) - F^*)^T W_i \cdot \big((F(\boldsymbol{A}) - F^*)\big). \tag{15}$$

In the above eqautions, N is the number of tests, N_i is the number of the experimental points in the i^{th} test, the term of $(F(\boldsymbol{A}) - F^*)$ represents the difference between simulated $F(\boldsymbol{A})$ and experimetal results F^*, and W_i is a weighting function/matrix for the i^{th} test.

Finally, the parameters for void coalescence were calibrated for the displacement after d_2 until

fracture. It should be noted that the material parameters for void coalescence are highly dependent on the parameters previously determined for void nucleation and growth. Therefore, careful calibration of material parameters should be performed repeatedly to achieve satisfactory results.

In this study, the GTN model parameters were first calibrated with the uniaxial tension experiment, and then the shear parameter kw in the GTN-shear model was determined while maintaining the GTN model parameters. It is worth mention that the best way to obtain the shear parameter kw is to accommodate the in-plane shear test because of low triaxiality [83]. The optimization result from the algorithm may not be the global solution as a conventional numerical algorithm was used in this study. Advanced method such as machine learning is known to achieve a global solution [87], and it requires further extensive investigations in future research.

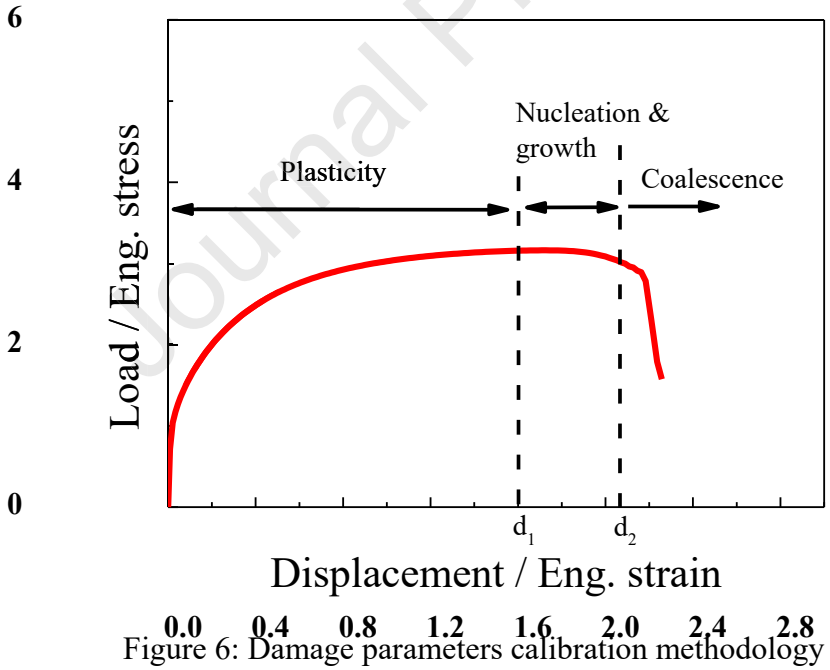

Figure 6: Damage parameters calibration methodology

Figure 7 shows a comparison of the engineering stress–strain curves obtained from uniaxial tensile tests and simulation using the GTN-type damage models. The corresponding material parameters are listed in Table 2. Results from both the GTN and GTN-shear models show good

agreement with experimental data in terms of the flow behavior, including post-necking and ultimate tensile strength. A small deviation in the displacement was observed at the onset of fracture in the numerical simulations, but the relative errors are insignificant, that is 0.7 % and 1.8 % for the GTN and GTN-shear models, respectively.

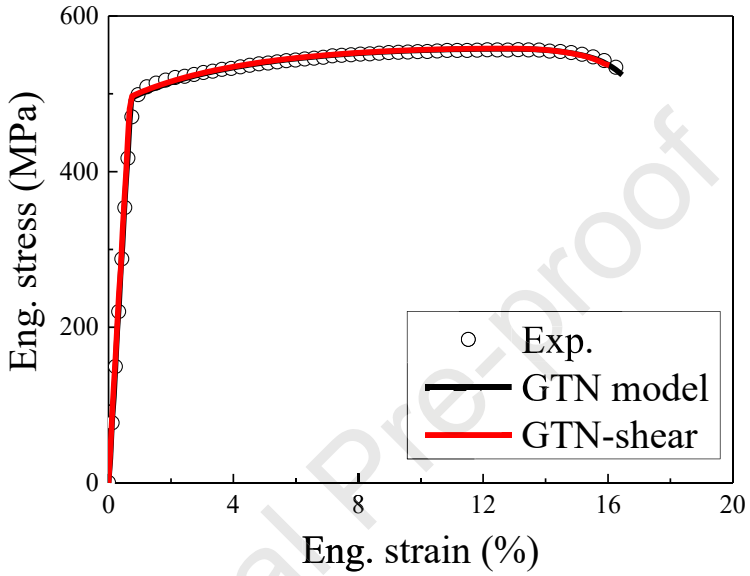

Figure 7: Comparison of engineering stress−strain curves obtained from uniaxial tension tests and from simulations using the GTN-type models.

Table 2: Material coefficients of the models

Swift hardening law in Eq. (2)							
K (MPa)		ε_0		n			
834.8		0.028		0.145			
GTN-shear model in Eqs. (3), (5), (9), and (11)							
q_1	q_2	f_N	S_N	ε_N	f_a	f_b	k_w
1.5	1.0	0.005	0.1	0.3	0.008	0.009	25.0

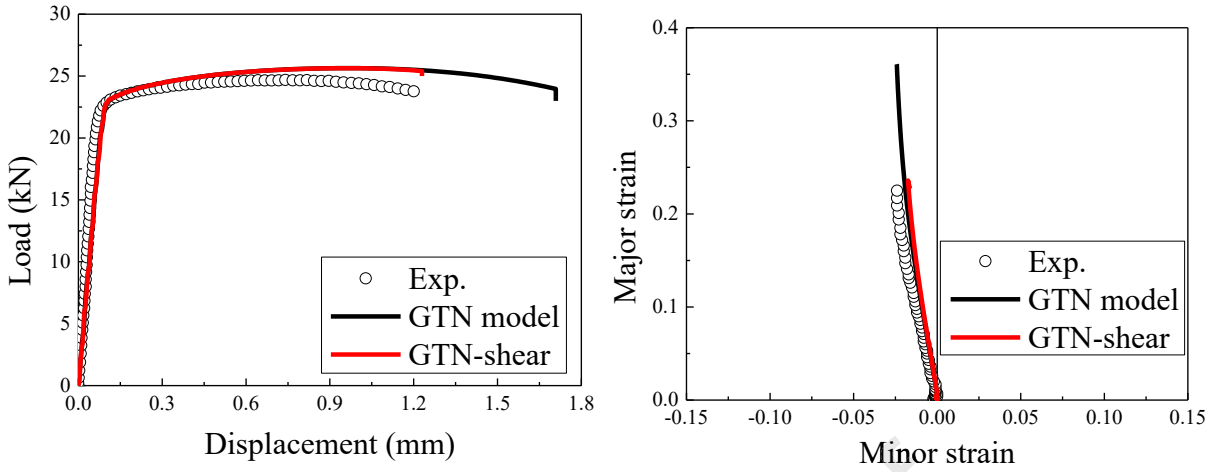

(a) (b)

Figure 8: Comparison of the PST experiment and simulations for (a) load−displacement curves, and (b) major−minor strain paths.

Figure 8 (a) shows a comparison of the load–displacement curves obtained from experiment and simulations using the GTN-type models. Both GTN-type models yielded reasonably good predictions for the load–displacement curves, particularly before the load maximum. However, a significant discrepancy was observed between the GTN and GTN-shear models in the prediction of displacement at the onset of fracture, as shown in the figure. Some experimental and simulation results are: 24.9 kN (average value obtained from the experiments, with a standard deviation of 0.19 kN), 26.2 kN (GTN), and 25.6 kN (GTN-shear) at the maximum load; 1.17 mm (average value obtained from the experiments, with a standard deviation of 0.03 mm), 1.71 mm (GTN), 1.23 mm (GTN-shear) for displacement at the onset of failure.

The simulation and experimental results of the strain paths of the major and minor strain components on the sheet surface were compared, as shown in Figure 8 (b). The experimental results demonstrate a linear strain path behavior and nearly plane strain deformation, and the corresponding numerical results obtained from both GTN-type models showed good agreement except for the over-estimated fracture strain level of the GTN model.

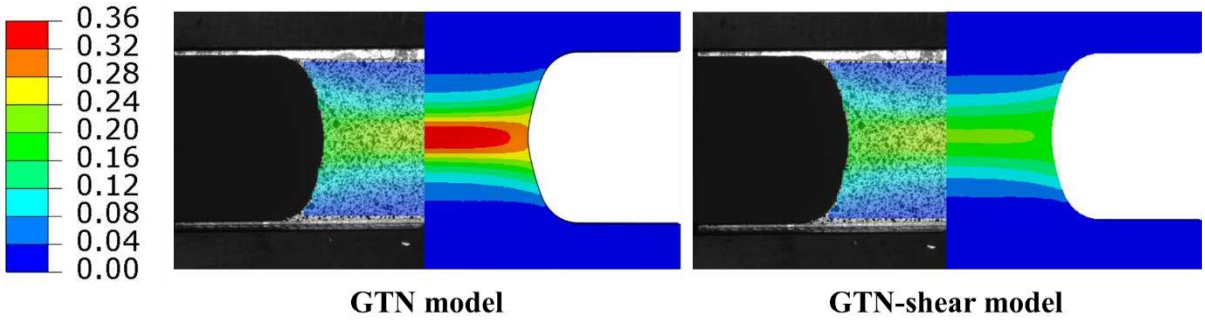

(a)

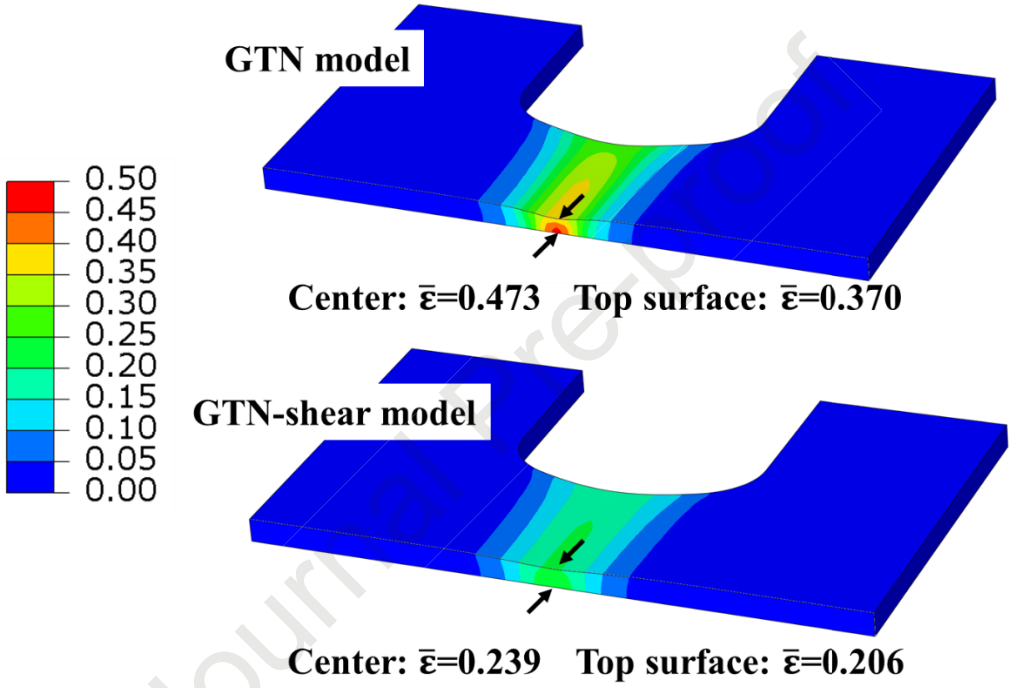

(b)

Figure 9: (a) Comparison of the major strain field on the surface obtained from experiments and simulation, and (b) FE predictions of the equivalent strain through the thickness at the initiation of fracture in the PST tests.

The surface strain distribution obtained using DIC at the onset of fracture was also compared with FE simulation results, as shown in Figure 9 (a). The figures on the left represent the full strain field of the major strain during the experiments. A sharper strain gradient in the middle of the specimen was observed in the same direction as the fracture propagation. When the simulation results were overlaid with the experimental data, the contours and strain levels

matched well with the GTN-shear model prediction, whereas they were overpredicted with the GTN model. Figure 9 (b) shows the equivalent strain distributions predicted by each model. The GTN model predicted a higher equivalent strain level than the GTN-shear model, with strong localization in the gauge and a severe strain gradient in the thickness direction. It can be concluded from these results that the ductile damage behavior in plane strain tension deformation is predicted more reliably using the GTN-shear model than using the GTN model.

4.2. Plane strain deformation from the LDH tests

Figure 10 (a) and (b) show a comparison of the punch load–stroke curves and strain evolution obtained from experiment and simulation, respectively during LDH tests for plane strain deformation. As shown in Figure 10 (a), the GTN-shear model accurately predicted the punch stroke to fracture, whereas the punch load was slightly overestimated. However, the GTN model overestimated the punch load and displacement at the onset of fracture. The strain path evolution during LDH tests was also accurately predicted by both GTN-type models before the onset of material fracture, as shown in Figure 10 (b). However, similar to Figure 10 (a), the GTN model could not accurately predict the strain path evolution at the onset of fracture; these trends agree with those previously discussed.

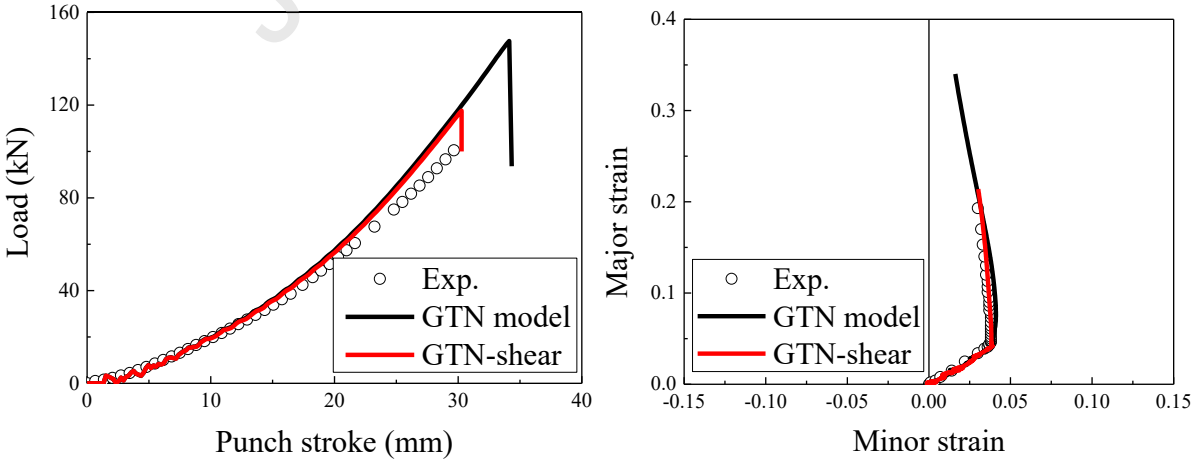

(a) (b)

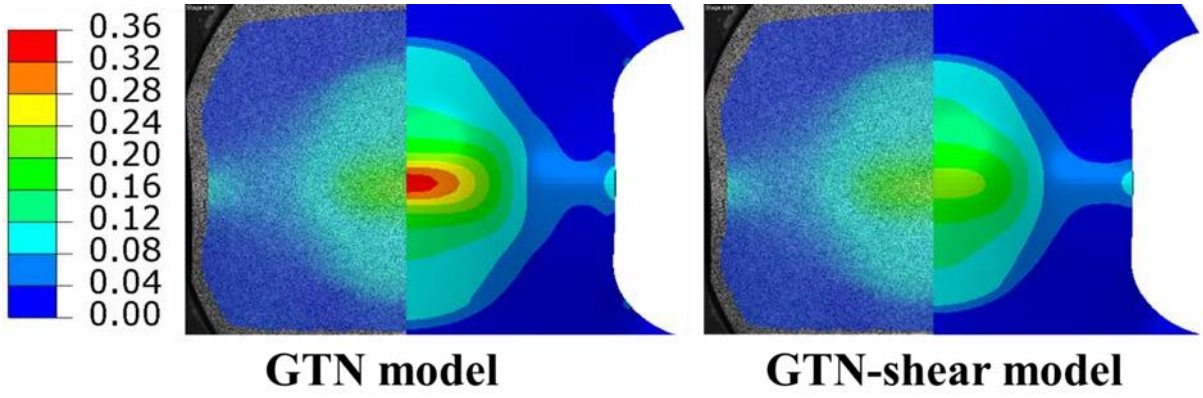

(c)

Figure 10: Comparison of the experimental and simulation results from the LDH tests: (a) punch load−stroke plots, (b) major–minor strain path, and (c) major strain distribution at the onset of fracture.

Furthermore, the results of the major strain distribution at the onset of fracture predicted using the GTN-type models were compared with experimental results, as shown in Figure 10 (c). The GTN model over-estimated the major strain at the pole with a value of 0.36, whereas the GTN-shear model can reproduce the experimentally measured values with minimal error. The results are qualitatively similar to those obtained from earlier simulations of PST tests.

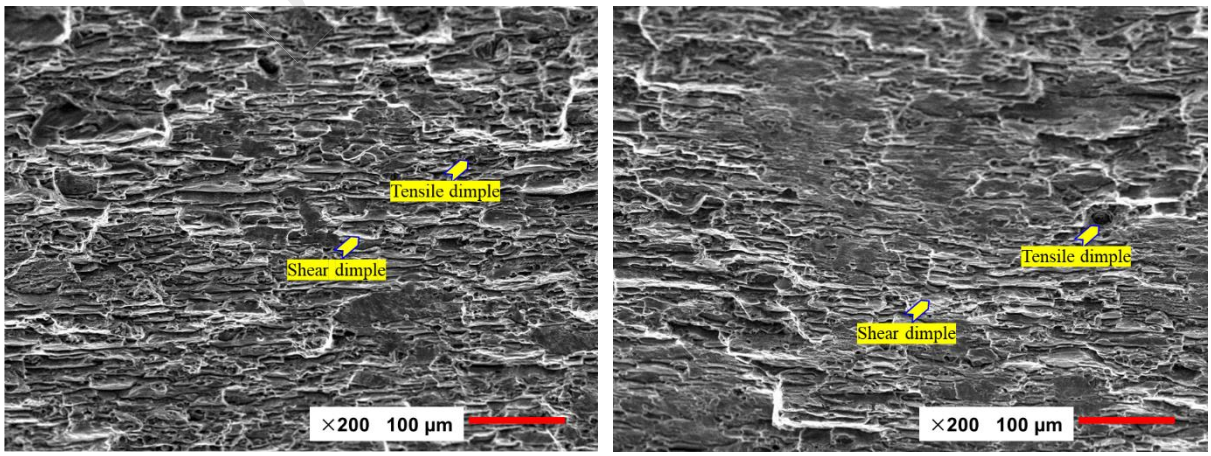

(a) (b)

Figure 11: Fractured morphology (200×) of (a) LDH with W100 specimens and (b) PST tests.

The fracture surfaces of the AA 7075-T6 sheets subjected to two different plane strain deformation modes, namely, PST and LDH tests, were observed using a scanning electron microscope (SEM). The representative fractographies of the LDH and PST tests are shown in Figure 11 (a) and (b), respectively. A comparison of the two figures show that a deeper and greater number of dimples can be observed for LDH than for PST tests. However, the fractographies for both plane strain deformation results show that some dimples were formed in a particular direction, such as shear dimples induced by inter-void shearing. This demonstrates the critical role of the shear term in the damage models and validates the good agreement between the GTN-shear model predictions and experimental results.

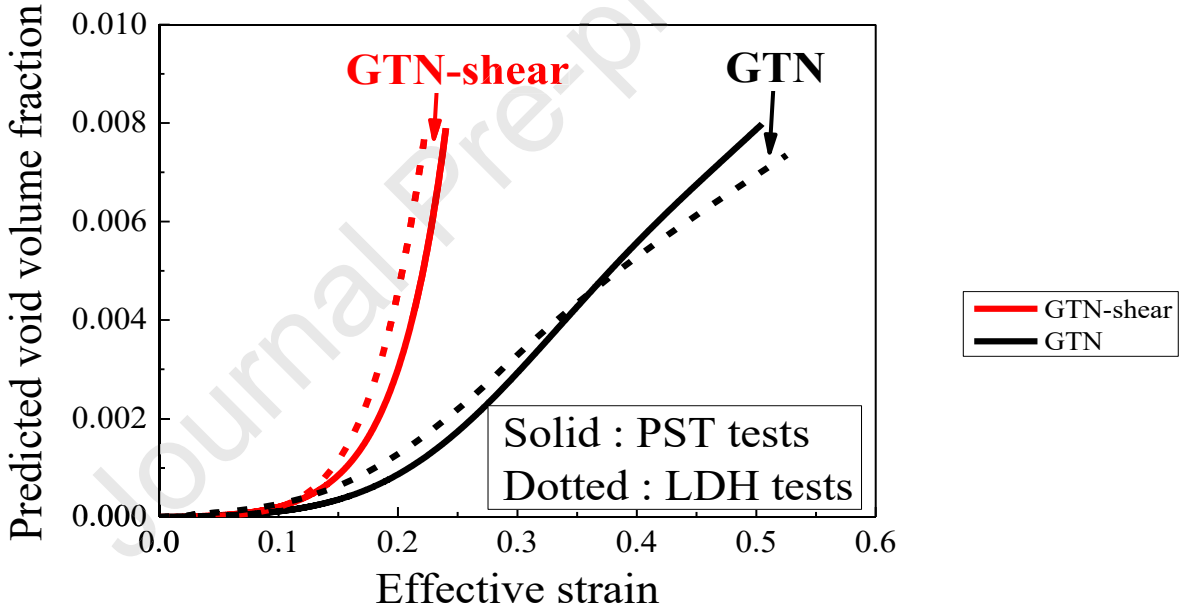

Figure 12: Comparison of the predicted total void volume fraction for PST and LDH tests obtained from GTN and GTN-shear models.

Figure 12 shows the total void volume fraction (VVF) at the critical elements for GTN and GTN-shear models in the FE simulations. The comparison indicates that inter-void shearing effect clearly plays a role in the prediction of the total VVF. The total VVF rate was similar for both damage models before an effective strain of 0.1, whereas the GTN-shear model yielded a

rapid increase in the total VVF after an effective strain of 0.1. Therefore, material failure occurred earlier in the GTN-shear model for both simulations. In contrast, a lower total VVF rate evolution was observed in the GTN model, which resulted in discrepancy in the prediction of the material failure behavior compared with experimental results.

4.3. V-die air bending tests

The experimental results of the V-die air bending test were compared with simulation results from the GTN and GTN-shear models in which the parameters were characterized using a simple tension experiment. The experimental and simulation results of the punch load–displacement curves were compared, as shown in Figure 13. The FE simulation results of the punch load–displacement curves for both damage models showed good agreement with experimental data, indicating that the damage models have an insignificant effect on the prediction of the punch load in the V-die bending tests.

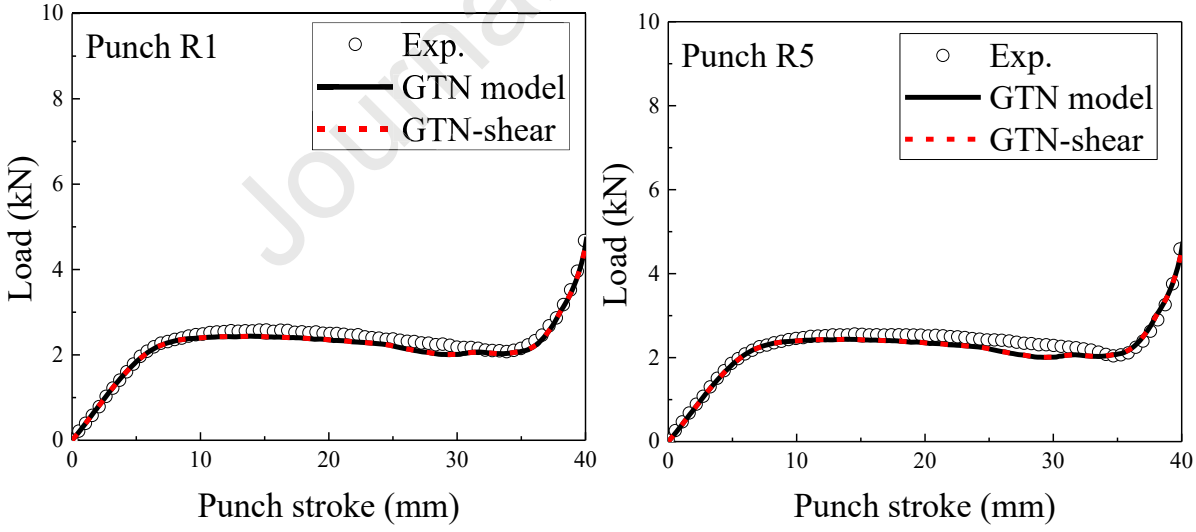

(a) (b)

Figure 13: Comparison of the punch load–stroke curves obtained from experiment and simulation for a punch radius of (a) 1 mm, and (b) 5 mm.

Figure 14 (a) and (b) show the optical measurement results for the V-die air bending tests for punch radii of 1 mm and 5 mm, respectively. As shown in the figures, material fracture was observed in the experiment with a punch radius of 1 mm, but not in that with a punch radius of 5 mm. The corresponding simulation results for the GTN-shear models are shown in Figure 14 (c) and (d), and the effective strain distribution is illustrated. For a punch radius of 1 mm, the fracture initiation at the outer surface was predicted in the simulation, which seems to agree with the experimental observations in Figure 14 (a). For a punch radius of 5 mm, the simulation results for the GTN-shear model did not show any material failure after the V-die bending tests, which is similar to the result from the experiment.

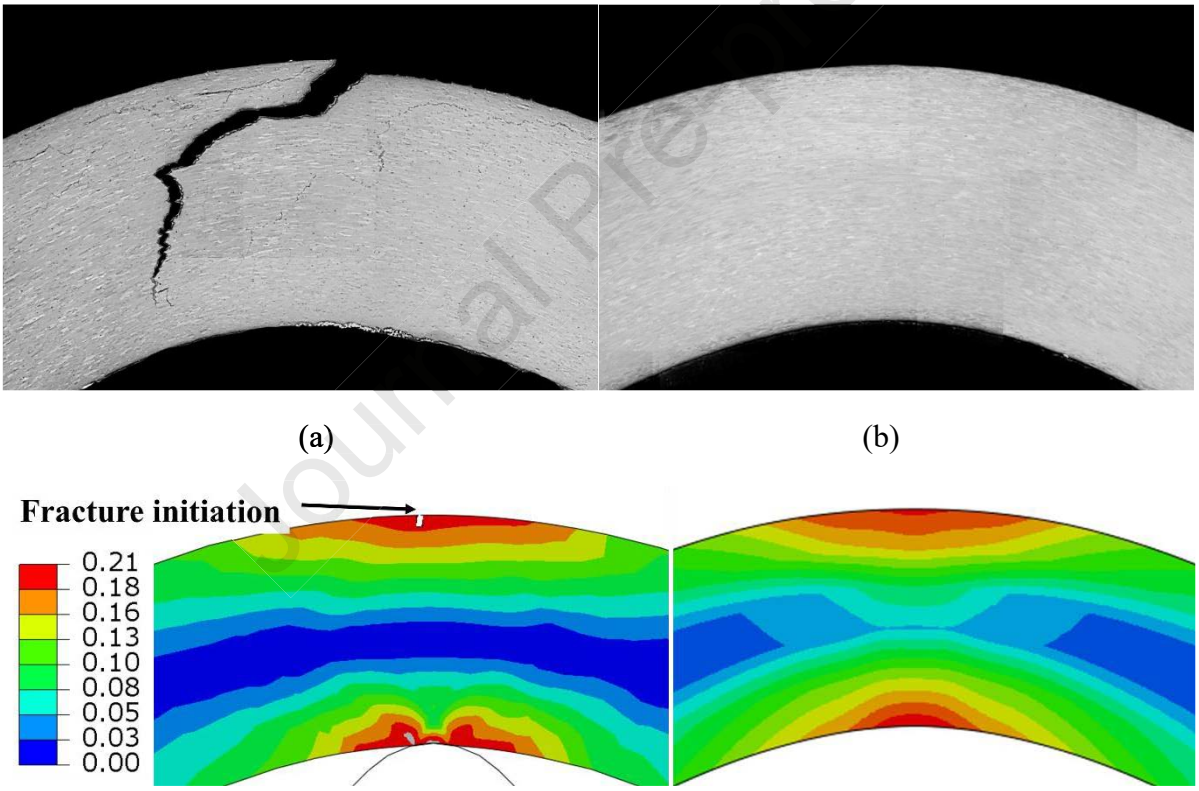

Figure 14: Optical measurement results after V-bending tests for a punch radius of (a) 1 mm, and (b) 5 mm, and the corresponding simulation results (c) and (d) for the GTN-shear model. The distribution of the effective strain is shown in the figure.

The predicted effective strains of the material fracture at the critical element using the GTN-shear model are shown in Figure 15 (a) and (b) with respect to the stress triaxiality and Lode angle function $\omega(\theta)$, respectively. As shown in Figure 15 (a), the stress triaxialities of the PST and V-die bending tests were fairly constant during deformation, whereas the LDH test reproduced some nonlinearity in the stress triaxiality during the tests. The stress triaxialities of the FE models for the critical elements at the onset of fracture are 0.5, 0.56, and 0.55 for the LDH, PST, and V-die bending tests, respectively. Therefore, the deformation modes in the three experiments were approximately in plane strain. In these plots, the average values of the stress triaxiality or the Lode angle function during loading are represented by dotted lines.

Regarding the Lode angle function $\omega(\theta)$, severe nonlinear curves were observed for the LDH and PST tests, as shown in Figure 15 (b). For the V-die bending tests, a linear loading path was obtained at an effective strain of 0.05. The values of the Lode angle function for all the samples at the onset of fracture are 0.75, 0.78, and 1.0 for the LDH, PST, and V-die bending tests, respectively. The difference in the Lode angle function value resulted in a difference in the final effective strain at the onset of fracture in the three experiments. This comparison represents different degrees of inter-void shearing effect on the fracture behavior due to the effect of the Lode angle, even though the stress triaxiality values of the three experiments are nearly plane strain deformation.

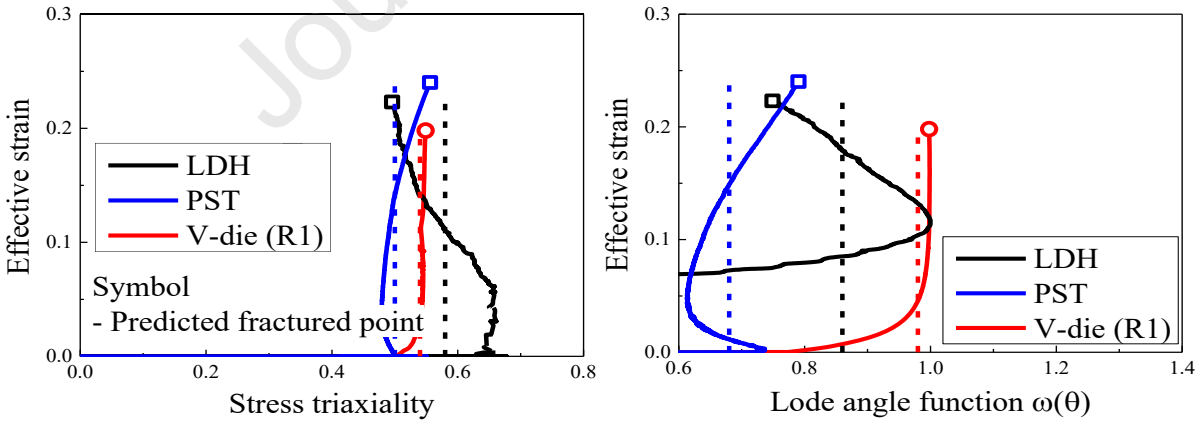

(a) (b)

Figure 15: Effective strain of the fracture prediction of the GTN-shear model with respect to the (a) stress triaxiality and (b) Lode angle function. The symbol represents the fractured point and the dotted lines are the average values during loading.

The predicted the void volume fractions at a critical element from the simulations are illustrated in Figure 16. Figure 16 (a) shows the prediction of void volume fraction using the original GTN and GTN-shear models in V-die air bending tests. The GTN-shear model predicts increased void volume fraction from the inter-void shearing, originated from the Lode angle in Figure 15 (b). Similarly, the pronounced void volume fraction induced by inter-void shearing is observed in the PST and LDH tests as shown in Figure 16 (b) and (c). This observation explains the improved predictive capability of the material failure for the GTN-shear model under plane strain deformation.

It is also worth noting that the UT simulation presents the void volume fraction originated by the inter-void shearing effect, as shown in Figure 16 (d). Theoretically, the stress triaxiality and Lode angle function for the case of uniaxial tension were expected to be $\frac{1}{3}$ and 0, respectively, indicating the absence of void volume fraction from inter-void shearing. However, the occurrence of the necking caused by the plastic instability led to an arbitrary multiaxial stress state, resulting in the Lode angle function no longer being 0.

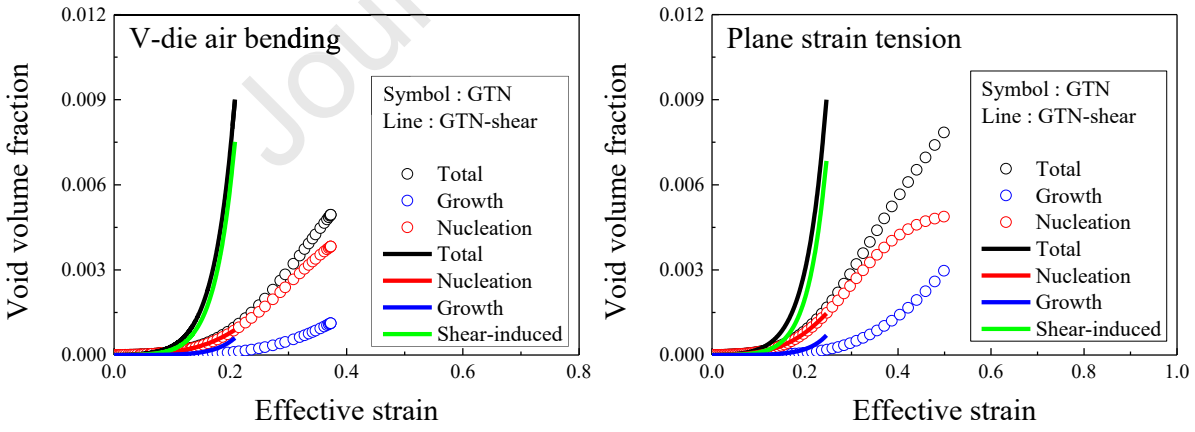

(a) (b)

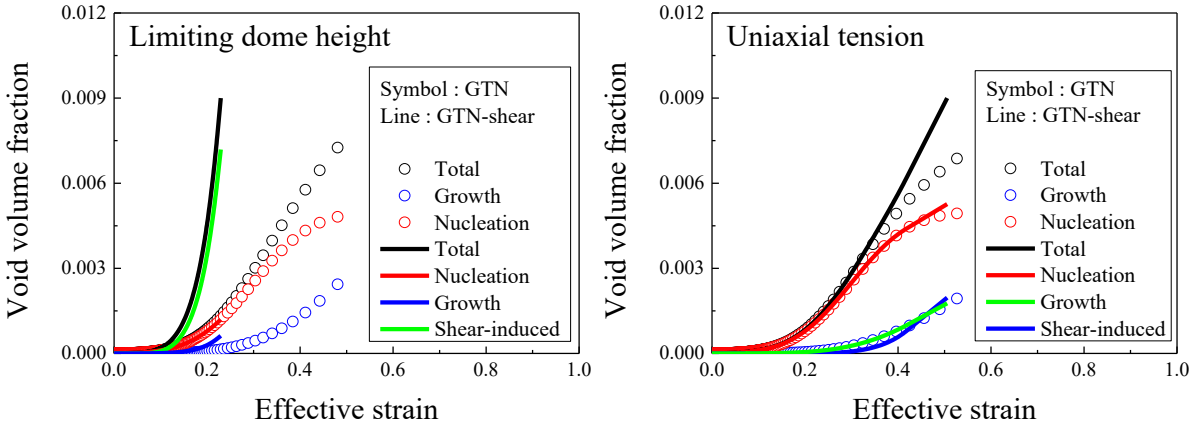

(c) (d)

Figure 16: Evolution of the void volume fraction for (a) UT, (b) PST, (c) LDH, and (d) V-die air bending tests.

4.4. Application of the damage model to virtual roll forming

This section presents the application of the GTN and GTN-shear models to industrial roll forming for the AA7075-T6 sheet sample. The V-channel part was virtually formed with five forming stations (see Figure 17), and driving rolls with a diameter of 140 mm and an interstation distance of 305 mm were used as proposed in [12]. The virtual roll forming process was modeled using ABAQUS/Explicit commercial software, and the springback analysis was not included in this study. The rolls were modeled as an analytical rigid body. The blank sheet size was 500 × 20 mm^2 (length × width) considering the half-symmetric condition, and the blank was discretized using reduced integration eight-node hexahedral elements (C3D8R). Five elements were used through the material thickness, and a refined element with a size of 5 × 0.4 mm^2 (length × width) was applied to the critical bending area. A friction coefficient of 0.2 was used in the simulations.

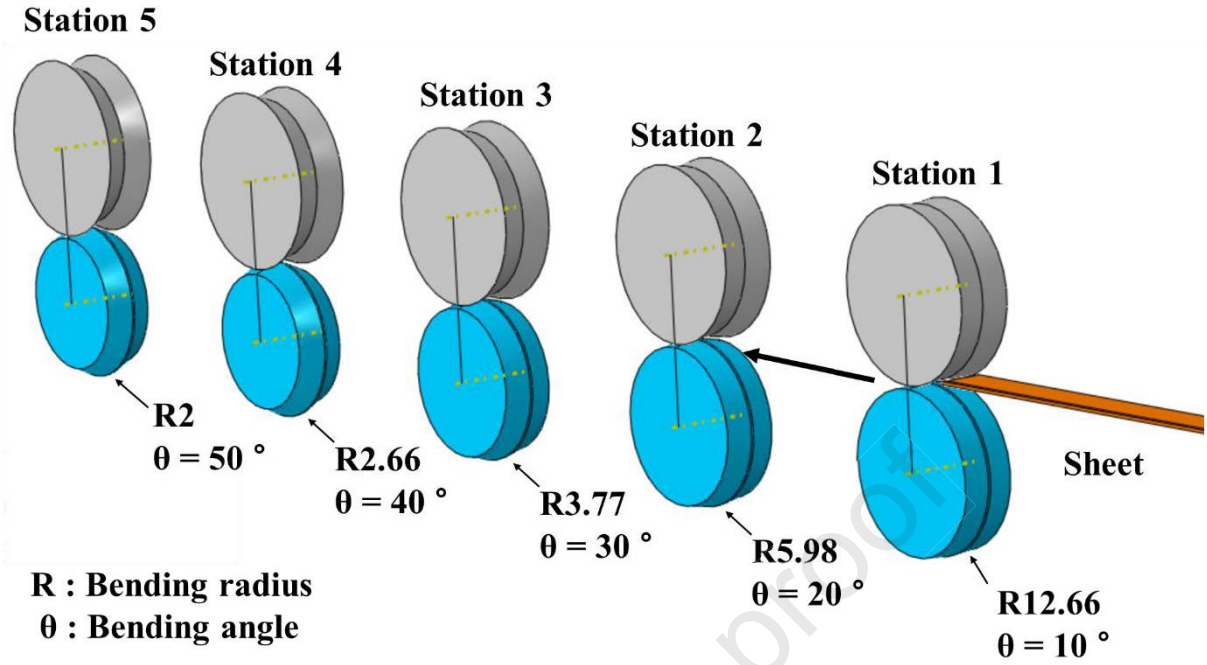

Figure 17: FE model of virtual roll forming

The FE results of the virtual roll forming process using the GTN-shear model are shown in Figure 18. As expected, the AA 7075-T6 sample fractured after Station 4 of the virtual roll forming process. However, no material failure was predicted in the original GTN model because the effective strain at the onset of material fracture under plane strain deformation was much higher than that of the GTN-shear model, as discussed earlier. The current FE results of the GTN-shear model show that the micromechanics-based damage model can be utilized to simulate the complex forming process.

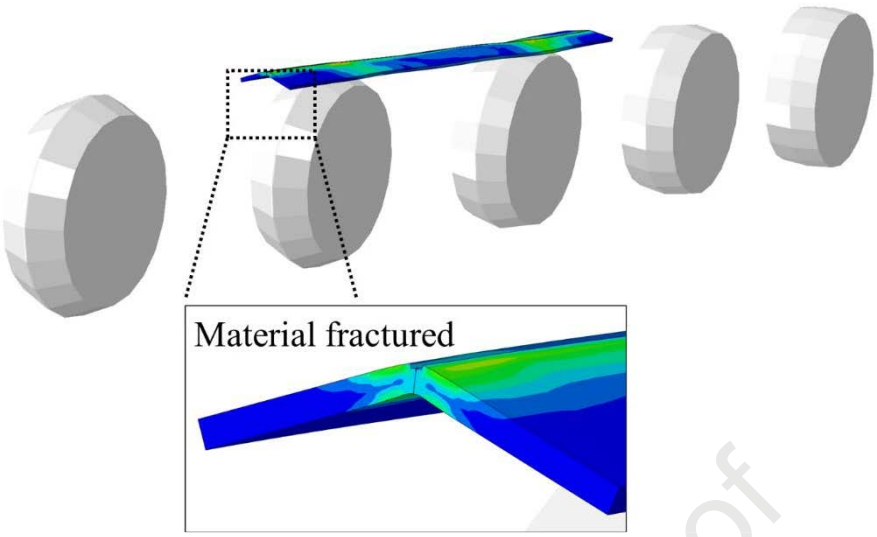

Figure 18: Simulation results of the virtual roll forming process using the GTN-shear model

A more detailed analysis of the virtual roll forming simulations was performed, as shown in Figure 19. A clear deviation from the average stress triaxiality can be observed in Figure 19 (a) owing to the complex loading history, including unloading during the forming process; however, plane strain deformation is mainly expected (stress triaxiality = 0.577) at the bending dominant deformation regions in the roll forming process. Figure 19 (b) shows a comparison of the predicted void volume fractions from the GTN and GTN-shear models. An insignificant difference in the VVF predictions obtained from the two models is observed in Stations 1 and 2 during rolling, as shown in the figure. However, as the bending radius became sharper after rolling at Station 3, a dramatic increase in the void volume fraction of the GTN-shear model occurred owing to the inter-void shearing effect, whereas that of the GTN model did not increase.

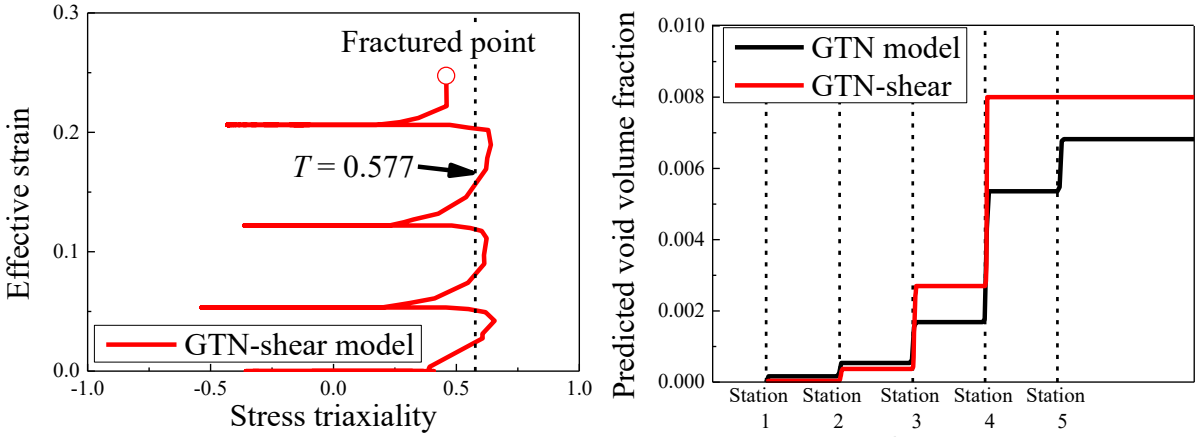

(a) (b)

Figure 19: FE results of a representative element selected on the critical bending line using the GTN-shear model for the (a) strain path evolution and (b) predicted void volume fraction.

5. Summary and conclusions

In this study, the ductile fracture of AA 7075-T6 sheets under plane strain deformation was investigated using an enhanced damage model that considers the inter-void shearing effect in the void evolution, namely, the GTN-shear model. UT tests were conducted to characterize the plastic strain-hardening behavior of the AA 7075-T6 sheet. Three different experiments representing the plane strain deformation mode were conducted, namely PST with notch, LDH, and V-die air bending tests. In addition, detailed fractography analysis was performed. FE simulations corresponding to the experiment were performed using the GTN and GTN-shear models. The material parameters of the damage models were determined by fitting the load–displacement curves experimentally obtained from the UT and PST tests. The LDH test results were then compared with those obtained from simulations using the GTN and GTN-shear models. In addition, the V-die air bending test results were compared in terms of the strain at the onset of fracture and the loading history with respect to the stress triaxiality and Lode angle. Finally, a virtual roll forming simulation was performed using the GTN-shear model to examine the ductile fracture behavior of the micromechanics-based damage models in an industrial application. The major findings of this study are summarized below.

- The GTN-shear model can reproduce the plasticity and ductile damage behaviors of the UT and PST tests, thereby capturing the load history and ductility limit in the corresponding FE simulations. In particular, the inter-void shearing effect should be considered in plane strain deformation simulations to accurately predict the ductile damage behavior.

- The original GTN model could not accurately capture the ductility limit of AA 7075-T6 in PST, LDH, and V-die air-bending tests. All the FE simulations overestimated the maximum load and displacement at the onset of fracture. In contrast, the simulation results obtained using the proposed GTN-shear model showed good agreement with experimental data in terms of the load–displacement curves and ductility. The results highlight the importance of inter-void shearing effect in the simulation of the plane strain deformation mode.

- Fractographic analysis of the PST and LDH tests was performed. Dimples corresponding to the classical ductile fracture mechanisms were observed from two

different plane strain deformation tests. In addition, some dimples formed in a particular direction were observed for both samples, leading to a clear inter-void shearing coalescence behavior.

- The loading paths in terms of the stress triaxiality and Lode angle function were analyzed from the FE simulations of three plane strain deformation tests, that is, PST, LDH, and V-die air bending. In the three tests, the predicted stress triaxiality values were similar, whereas the Lode angle function $\omega(\theta)$ values varied. This indicates that the GTN-shear model can contribute to different degrees of inter-void shearing effect in the different plane strain deformation tests.

- A bending-dominant process such as roll forming can be accurately simulated using the GTN-shear model, whereas prediction using the original GTN model was not very accurate. This implies that the inter-void shearing effect plays an important role in predicting material failure and is highly recommended for industrial applications. Experimental validation of the industrial forming problem will be carried out in future research.

Acknowledgments

J. Ha appreciates the support of the New Hampshire Center for Multiscale Modeling and Manufacturing of Biomaterials (NH BioMade) project provided by the US National Science Foundation (NSF) EPSCoR award (#1757371). H. J. Bong appreciates the support by the Fundamental Research Program of the Korea Institute of Materials Science (KIMS, PNK9460). Finally, this research was supported by “Regional Innovation Strategy (RIS)” through the National Research Foundation of Korea (NRF) funded by the Ministry of Education (MOE) (2021RIS-002 and 2021RIS-003).

Conflict of interest

The authors declare that they have no known competing financial interests or personal relationships that could have appeared to influence the work reported in this paper.

Appendix A: Finite element implementation of the enhanced damage model

A stress-updating algorithm for the GTN-shear model was formulated using the generalized backward Euler return mapping algorithm [50,88] and implemented in the commercial FE software ABAQUS/Explicit via a user-defined material subroutine (VUMAT) [77,89]. For a given total strain increment $\Delta\boldsymbol{\varepsilon}$ at time t + Δt, the stress and state variables must be updated. The total strain increment is divided into two strain increments, as follows:

$$\Delta\boldsymbol{\varepsilon} = \Delta\boldsymbol{\varepsilon}^{\mathrm{el}} + \Delta\boldsymbol{\varepsilon}^{\mathrm{pl}} \tag{A.1}$$

where $\Delta\boldsymbol{\varepsilon}^{\mathrm{el}}$ and $\Delta\boldsymbol{\varepsilon}^{\mathrm{pl}}$ are the elastic and plastic strain increments, respectively.

The elasticity equation is given as

$$\boldsymbol{\sigma}_{\mathrm{t}+\Delta\mathrm{t}} = \boldsymbol{\sigma}^{\mathrm{el}} - \mathbf{C}\colon\Delta\boldsymbol{\varepsilon}^{\mathrm{pl}}, \tag{A.2}$$

where $\boldsymbol{\sigma}^{\mathrm{el}}$ is the elastic predictor defined as

$$\boldsymbol{\sigma}^{\mathrm{el}} = \mathbf{C}\colon\left(\boldsymbol{\varepsilon}_{\mathrm{t}}^{\mathrm{el}} + \Delta\boldsymbol{\varepsilon}\right), \tag{A.3}$$

where $\boldsymbol{\varepsilon}_{\mathrm{t}}^{\mathrm{el}}$ is the total elastic strain at time t and $\mathbf{C}$ is the fourth-order linear isotropic elasticity tensor expressed as

$$\mathbf{C} = 2G\mathbf{I}_4 + \left(K - \frac{2}{3}G\right)\mathbf{I}\otimes\mathbf{I}\,, \tag{A.4}$$

G and *K* are the shear and bulk moduli, respectively, and $\mathbf{I}_4$ and $\mathbf{I}$ are the fourth- and second-order identity tensors, respectively.

The following equations are the yield function, associated flow rule, and evolution of state variables:

$$\Phi(\boldsymbol{\sigma}_{\mathrm{t}+\Delta\mathrm{t}}, H^{\alpha}_{\mathrm{t}+\Delta\mathrm{t}}) = 0\,, \tag{A.5}$$

$$\Delta\boldsymbol{\varepsilon}^{\mathrm{pl}} = \frac{1}{3}\Delta\varepsilon_p\mathbf{I} + \Delta\varepsilon_q\mathbf{n}_{\mathrm{t}+\Delta\mathrm{t}}\,, \tag{A.6}$$

$$\Delta H^{\alpha} = \bar{h}\left(\Delta\boldsymbol{\varepsilon}^{\mathrm{pl}}, \boldsymbol{\sigma}_{\mathrm{t+\Delta t}}, H^{\beta}_{\mathrm{t+\Delta t}}\right), \tag{A.6}$$

$$\mathbf{n}_{\mathrm{t+\Delta t}} = \left(\frac{\partial \sigma_{\mathrm{e}}}{\partial \boldsymbol{\sigma}}\right)_{\mathrm{t+\Delta t}},\ \Delta\varepsilon_p = -\Delta\gamma\left(\frac{\partial \Phi}{\partial p}\right)_{\mathrm{t+\Delta t}},\ \Delta\varepsilon_q = \Delta\gamma\left(\frac{\partial \Phi}{\partial q}\right)_{\mathrm{t+\Delta t}}, \tag{A.7}$$

where $\Delta\gamma$ is the plastic multiplier, p is the hydrostatic pressure, and q is the effective stress. H^{α} (α = 1 and 2) is the state variable of the effective strain $\bar{\varepsilon}$ and porosity f.

Removing the plastic multiplier $\Delta\gamma$ in Eq. (A.7) yields the following equation:

$$\Delta\varepsilon_p\left(\frac{\partial \Phi}{\partial q}\right)_{\mathrm{t+\Delta t}} + \Delta\varepsilon_q\left(\frac{\partial \Phi}{\partial p}\right)_{\mathrm{t+\Delta t}} = 0. \tag{A.8}$$

By substituting Eq. (A.6) into Eq. (A.2),

$$\boldsymbol{\sigma}_{\mathrm{t+\Delta t}} = \boldsymbol{\sigma}^{\mathrm{el}} - K\Delta\varepsilon_p\mathbf{I} - 2\mathrm{G}\Delta\varepsilon_q\mathbf{n}_{\mathrm{t+\Delta t}}. \tag{A.9}$$

Using Eq. (A.9), the complex nonlinear equations were reduced to two equations with respect to the scalar values of $\Delta\varepsilon_p$ and $\Delta\varepsilon_q$ as follows:

$$\Phi(p_{\mathrm{t+\Delta t}}, q_{\mathrm{t+\Delta t}}, H^{\alpha}_{\mathrm{t+\Delta t}}) = 0\,, \tag{A.10}$$

$$\Delta\varepsilon_p\left(\frac{\partial \Phi}{\partial q}\right)_{\mathrm{t+\Delta t}} + \Delta\varepsilon_q\left(\frac{\partial \Phi}{\partial p}\right)_{\mathrm{t+\Delta t}} = 0\,, \tag{A.11}$$

where

$$p_{\mathrm{t+\Delta t}} = p^{\mathrm{el}} + K\Delta\varepsilon_p \tag{A.12}$$

$$q_{\mathrm{t+\Delta t}} = q^{\mathrm{el}} - 3G\Delta\varepsilon_q \tag{A.13}$$

$$\Delta H^{\alpha} = \bar{h}\left(\Delta\varepsilon_p, \Delta\varepsilon_q, p, q, H^{\beta}_{\mathrm{t+\Delta t}}\right). \tag{A.14}$$

Eqs. (A.10) and (A.11) were solved using Newton's method. Additional details on the implementation of this method can be found in [90].

Appendix B: Influence of friction coefficient on the ductility predictions

To investigate the friction effect on ductility, five simulations using the GTN-shear model with friction coefficients of fc = 0.01 and 0.03 for the LDH and fc = 0.02, 0.1, and 0.2 for the V-air die bending tests with punch radius of 1 mm were performed. These values were selected in the practical range of friction coefficients for cold sheet forming with/without the lubrication.

Figure B.1 shows the effect of friction on the ductility prediction. For the LDH tests, the lower friction coefficient of 0.01 predicted the slightly higher punch stroke at the onset of the fracture but the difference is negligible. In the V-die air bending tests, the predicted loads are highly sensitive to friction coefficients as described in Figure B.1 (b) while the punch stroke to fracture is similar for four difference friction coefficients (all predicted punch strokes to fracture were around 40.0 ± 0.014 mm). The comparison of simulated results shows that the referred friction coefficients, i.e., 0.02 and 0.15, are well validated.

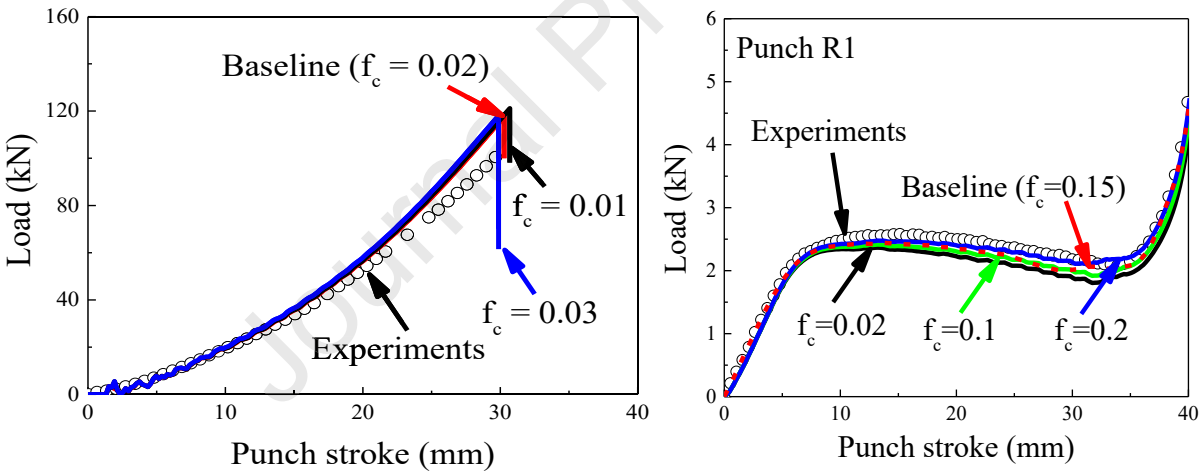

Figure B.1: Effect of friction coefficient in (a) LDH and (b) V-die air bending tests.

References

[1] Choi Y, Lee J, Panicker SS, Jin H-K, Panda SK, Lee M-G. Mechanical properties, springback, and formability of W-temper and peak aged 7075 aluminum alloy sheets: Experiments and modeling. Int J Mech Sci 2020;170:105344.

[2] LaDelpha ADP, Neubing H, Bishop DP. Metallurgical assessment of an emerging Al-Zn-Mg-Cu P/M alloy. Mater Sci Eng A 2009;520:105–13. https://doi.org/10.1016/j.msea.2009.05.039.

[3] Peng G, Chen K, Chen S, Fang H. Evolution of the second phase particles during the heating-up process of solution treatment of Al–Zn–Mg–Cu alloy. Mater Sci Eng A 2015;641:237–41. https://doi.org/https://doi.org/10.1016/j.msea.2015.06.058.

[4] Ma S, Sun Y, Wang H, Lü X, Qian M, Ma Y, et al. Effect of a Minor Sr Modifier on the Microstructures and Mechanical Properties of 7075 T6 Al Alloys. Met 2017;7. https://doi.org/10.3390/met7010013.

[5] Moon C, Thuillier S, Lee J, Lee M-G. Mechanical properties of solution heat treated Al-Zn-Mg-Cu (7075) alloy under different cooling conditions: Analysis with full field measurement and finite element modeling. J Alloys Compd 2021;856:158180. https://doi.org/https://doi.org/10.1016/j.jallcom.2020.158180.

[6] Lee J, Bong HJ, Kim D, Lee Y-S, Choi Y, Lee M-G. Application of Combined W-Temper and Cold Forming Technology to High-Strength Aluminum Alloy Automotive Parts. JOM 2019;71:4393–4404. https://doi.org/10.1007/s11837-019-03779-z.

[7] Lee J, Bong HJ, Kim D, Lee Y-S, Choi Y, Lee M-G. Mechanical Properties and Formability of Heat-Treated 7000-Series High-Strength Aluminum Alloy: Experiments and Finite Element Modeling. Met Mater Int 2020;26:682–694. https://doi.org/10.1007/s12540-019-00353-9.

[8] Taheri-Mandarjani M, Zarei-Hanzaki A, Abedi HR. Hot ductility behavior of an extruded 7075 aluminum alloy. Mater Sci Eng A 2015;637:107–22. https://doi.org/https://doi.org/10.1016/j.msea.2015.03.038.

[9] Hong J-H, Yoo D, Kwon YN, Kim D. Evaluation of rate-dependent forming limit for AA7075 sheets under pneumatic stretching method at elevated temperatures. J Mater Res Technol 2023;22:1839–54. https://doi.org/https://doi.org/10.1016/j.jmrt.2022.11.151.

[10] Choi Y, Lee J, Bong HJ, Lee M-G. Hole Expansion Characteristics of W-Tempered 7075 Aluminum Alloy Sheet in Comparison with Peak Aged T6 Tempered Alloy Sheet. Met Mater Int 2023;29:157–67. https://doi.org/10.1007/s12540-022-01201-z.

[11] Harrison NR, Luckey SG. Hot Stamping of a B-Pillar Outer from High Strength Aluminum Sheet AA7075. SAE Int J Mater Manf 2014;7:567–73. https://doi.org/10.4271/2014-01-0981.

[12] Deole AD, Barnett MR, Weiss M. The numerical prediction of ductile fracture of martensitic steel in roll forming. Int J Solids Struct 2018;144–145:20–31.

[13] Lee S, Lee J, Song J, Park J, Choi S, Noh W, et al. Fracture simulation of cold roll forming process for aluminum 7075-T6 automotive bumper beam using GISSMO damage model. Procedia Manuf 2018;15:751–8. https://doi.org/https://doi.org/10.1016/j.promfg.2018.07.314.

[14] Suckow T, Schroeder J, Groche P. Roll forming of a high strength AA7075 aluminum tube. Prod Eng 2021;15:573–86.

[15] Deb S, Panigrahi SK, Weiss M. Understanding material behaviour of ultrafine-grained aluminum nano-composite sheets with emphasis on stretch and bedning deformation. J Mater Process Technol 2021;293:117082.

[16] Andersen RG, Londono JG, Woelke PB, Nielsen KL. Fundamental differences between plane strain bending and far-field plane strain tension in ductile plate failure. J Mech Phys Solids 2020;141:103960. https://doi.org/https://doi.org/10.1016/j.jmps.2020.103960.

[17] Lundberg M, Melander A. Finite element analysis of roll forming of UHSS compared to traditional bending. IDDRG 2008 Int. Conf., 2008, p. 331–8.

[18] Park N, Huh H, Lim SJ, Lou Y, Kang YS, Seo MH. Fracture-based forming limit criteria for anisotropic materials in sheet metal forming. Int J Plast 2016;96:1–35.

[19] Lou Y, Yoon JW. Anisotropic ductile fracture criterion based on linear transformation. Int J Plast 2017;93:3–25. https://doi.org/https://doi.org/10.1016/j.ijplas.2017.04.008.

[20] Mu L, Zang Y, Wang Y, Li XL, Araujo Stemler PM. Phenomenological uncoupled ductile fracture model considering different void deformation modes for sheet metal forming. Int J Mech Sci 2018;141:408–23. https://doi.org/https://doi.org/10.1016/j.ijmecsci.2018.04.025.

[21] McClintock FA. A Criterion for Ductile Fracture by the Growth of Holes. J Appl Mech 1968;35:363–71.

[22] Lou Y, Huh H, Lim S, Pack K. New ductile fracture criterion for prediction of fracture forming limit diagrams of sheet metals. Int J Solids Struct 2012;49:3605–15.

[23] Rice JR, Tracey DM. On the ductile enlargement of voids in triaxial stress fields∗. J Mech Phys Solids 1969;17:201–17.

[24] Wierzbicki T, Bao Y, Lee Y-W, Bai Y. Calibration and evaluation of seven fracture models. Int J Mech Sci 2005;47:719–43.

[25] Bao Y, Wierzbicki T. On fracture locus in the equivalent strain and stress triaxiality space. Int J Mech Sci 2004;46:81–98.

[26] Bai Y, Wierzbicki T. A new model of metal plasticity and fracture with pressure and Lode dependence. Int J Plast 2008;24:1071–96.

[27] Mohr D, Marcadet SJ. Micromechanically-motivated phenomenological Hosford-Coulomb model for predicting ductile fracture initiation at low stress triaxialites. Int J Solids Struct 2015;67–68:40–55.

[28] Luo M, Dunand M, Mohr D. Experiments and modeling of anisotropic aluminum extrusions under multi-axial loading – Part II: Ductile fracture. Int J Plast 2012;32–33:36–58.

[29] Lee J, Kim S, Park H, Bong HJ, Kim D. Metal plasticity and ductile fracture modeling for cast aluminum alloy parts. J Mater Process Technol 2018;255:584–95.

[30] Bai Y, Wierzbicki T. Application of extended Mohr–Coulomb criterion to ductile fracture. Int J Fract 2010;161:1–20.

[31] Roth CC, Mohr D. Effect of strain rate on ductile fracture initiation in advanced high strength steel sheets: Experiments and modeling. Int J Plast 2014;56:19–44.

[32] Leclerc J, Nguyen V-D, Pardoen T, Noels L. A micromechanics-based non-local damage to crack transition framework for porous elastoplastic solids. Int J Plast 2020;127. https://doi.org/10.1016/j.ijplas.2019.11.010.

[33] Chen D, Li Y, Yang X, Jiang W, Guan L. Efficient parameters identification of a modified GTN model of ductile fracture using machine learning. Eng Fract Mech 2021;245. https://doi.org/10.1016/j.engfracmech.2021.107535.

[34] Lee J, Jong Bong H, Park H, Kim D. Micromechanics-based modeling of plastic and ductile fracture of aluminum alloy 2024-O. Eng Fract Mech 2022;261:108213. https://doi.org/10.1016/j.engfracmech.2021.108213.

[35] Gurson AL. Continuum theory of ductile rupture by void nucleation and growth. Part I: Yield criteria and flow rules for porous ductile media. ASME J Eng Mater Technol 1977;99:2–15.

[36] Chu CC, Needleman A. Void Nucleation Effects in Biaxially Stretched Sheets. J Eng Mater Technol 1980;102:249–56. https://doi.org/10.1115/1.3224807.

[37] Tvergaard V, Needleman A. Analysis of the cup-cone fracture in a round tensile bar. Acta Metall 1984;32:157–69.

[38] Needleman A, Tvergaard V. An analysis of ductile rupture in notched bars. J Mech Phys Solids 1984;32:461–90. https://doi.org/https://doi.org/10.1016/0022-5096(84)90031-0.

[39] Gao T, Ying L, Hu P, Han X, Rong H, Wu Y, et al. Investigation on mechanical behavior and plastic damage of AA7075 aluminum alloy by thermal small punch test:

Experimental trials, numerical analysis. J Manuf Process 2020;50:1–16. https://doi.org/https://doi.org/10.1016/j.jmapro.2019.12.012.

[40] Gholipour H, Biglari FR, Nikbin K. Experimental and numerical investigation of ductile fracture using GTN damage model on in-situ tensile tests. Int J Mech Sci 2019;164:105170. https://doi.org/https://doi.org/10.1016/j.ijmecsci.2019.105170.

[41] Chiyatan T, Uthaisangsuk V. Mechanical and fracture behavior of high strength steels under high strain rate deformation: Experiments and modelling. Mater Sci Eng A 2020;779:139125. https://doi.org/https://doi.org/10.1016/j.msea.2020.139125.

[42] Ali AN, Huang S-J. Ductile fracture behavior of ECAP deformed AZ61 magnesium alloy based on response surface methodology and finite element simulation. Mater Sci Eng A 2019;746:197–210. https://doi.org/https://doi.org/10.1016/j.msea.2019.01.036.

[43] Yang S, Ling X, Xue L. Application of small punch test to investigate mechanical behaviours and deformation characteristics of Incoloy800H. J Alloys Compd 2018;765:497–504.

[44] Allahverdizadeh N, Gilioli A, Manes A, Giglio M. An experimental and numerical study for the damage characterization of a Ti–6AL–4V titanium alloy. Int J Mech Sci 2015;93:32–47.

[45] Tang B, Wu F, Wang Q, Liu J, Guo N, Ge H, et al. Damage prediction of hot stamped boron steel 22MnB5 with a microscopic motivated ductile fracture criterion: Experiment and simulation. Int J Mech Sci 2020;169. https://doi.org/10.1016/j.ijmecsci.2019.105302.

[46] Nasir MW, Chalal H, Abed-Meraim F. Formability prediction using bifurcation criteria and GTN damage model. Int J Mech Sci 2021;191:106083. https://doi.org/https://doi.org/10.1016/j.ijmecsci.2020.106083.

[47] He Z, Zhu H, Hu Y. An improved shear modified GTN model for ductile fracture of aluminium alloys under different stress states and its parameters identification. Int J Mech Sci 2021;192:106081. https://doi.org/https://doi.org/10.1016/j.ijmecsci.2020.106081.

[48] Bong HJ, Kim D, Kwon YN, Lee J. Predicting hot deformation behaviors under multiaxial loading using the Gurson-Tvergaard-Needleman damage model for Ti–6Al–4V alloy sheets. Eur J Mech A/Solids 2021;87:104227. https://doi.org/10.1016/j.euromechsol.2021.104227.

[49] Nahshon K, Hutchinson JW. Modification of the Gurson Model for shear failure. Eur J Mech - A/Solids 2008;27:1–17. https://doi.org/10.1016/j.euromechsol.2007.08.002.

[50] Nahshon K, Xue Z. A modified Gurson model and its application to punch-out experiments. Eng Fract Mech 2009;76:997–1009.

[51] Xue L. Constitutive modeling of void shearing effect in ductile fracture of porous materials. Eng Fract Mech 2008;75:3343–66.

[52] Nielsen KL, Tvergaard V. Ductile shear failure or plug failure of spot welds modelled by modified Gruson model. Eng Fract Mech 2010;77:1031–47.

[53] Li WT, Cai ZY, Li H, Peng LF, Lai XM, Fu MW. The modified GTN-Thomason criterion for modelling of ductile fracture considering shear factor and size effect in micro-scaled plastic deformation. Int J Mech Sci 2021;204:106540. https://doi.org/https://doi.org/10.1016/j.ijmecsci.2021.106540.

[54] Madou K, Leblond J-B. A Gurson-type criterion for porous ductile solids containing arbitrary ellipsoidal voids—II: Determination of yield criterion parameters. J Mech Phys Solids 2012;60:1037–58. https://doi.org/https://doi.org/10.1016/j.jmps.2012.01.010.

[55] Madou K, Leblond J-B, Morin L. Numerical studies of porous ductile materials containing arbitrary ellipsoidal voids – II: Evolution of the length and orientation of the void axes. Eur J Mech - A/Solids 2013;42:490–507. https://doi.org/https://doi.org/10.1016/j.euromechsol.2013.06.005.

[56] Gologanu M, Leblond J-B, Devaux J. Approximate models for ductile metals containing non-spherical voids—Case of axisymmetric prolate ellipsoidal cavities. J Mech Phys Solids 1993;41:1723–54. https://doi.org/https://doi.org/10.1016/0022-5096(93)90029-F.

[57] Castañeda PP, Zaidman M. Constitutive models for porous materials with evolving microstructure. J Mech Phys Solids 1994;42:1459–97. https://doi.org/https://doi.org/10.1016/0022-5096(94)90005-1.

[58] Aravas N, Ponte Castañeda P. Numerical methods for porous metals with deformation-induced anisotropy. Comput Methods Appl Mech Eng 2004;193:3767–805. https://doi.org/https://doi.org/10.1016/j.cma.2004.02.009.

[59] Danas K, Ponte Castañeda P. A finite-strain model for anisotropic viscoplastic porous media: II – Applications. Eur J Mech - A/Solids 2009;28:387–401. https://doi.org/https://doi.org/10.1016/j.euromechsol.2008.11.003.

[60] Danas K, Ponte Castañeda P. A finite-strain model for anisotropic viscoplastic porous media: I – Theory. Eur J Mech - A/Solids 2009;28:387–401. https://doi.org/https://doi.org/10.1016/j.euromechsol.2008.11.002.

[61] Woelke PB. Simplification of the Gurson model for large-scale plane stress problems. Int J Plast 2020;125:331–47. https://doi.org/10.1016/j.ijplas.2019.10.004.

[62] Jeong W, Kim C, Lee C-A, Bong HJ, Hong S-H, Lee M-G. A probabilistic mean-field and microstructure based finite element modeling for predicting mechanical and ductile fracture behavior of the cast aluminum alloy. Int J Plast 2022;154:103299. https://doi.org/https://doi.org/10.1016/j.ijplas.2022.103299.

[63] Nielsen KL, Tvergaard V. Effect of a shear modified Gurson model on damage development in a FSW tensile specimen. Int J Solids Struct 2009;46:587–601. https://doi.org/https://doi.org/10.1016/j.ijsolstr.2008.09.011.

[64] Hong J-H, Kim H, Han S, Kwon Y-N, Park H, Kim D. Bendability assessment of high strength aluminum alloy sheets via V-die air bending method. J Mater Res Technol 2022;20:1481–94. https://doi.org/10.1016/j.jmrt.2022.07.123.

[65] Zhang J, Kalnaus S, Behrooz M, Jiang Y. Effect of Loading History on Stress Corrosion Cracking of 7075-T651 Aluminum Alloy in Saline Aqueous Environment. Metall Mater Trans A 2011;42:448–60. https://doi.org/10.1007/s11661-010-0419-8.

[66] Harrison TJ, Crawford BR, Janardhana M, Clark G. Differing microstructural properties of 7075-T6 sheet and 7075-T651 extruded aluminium alloy. Procedia Eng 2011;10:3117–21. https://doi.org/https://doi.org/10.1016/j.proeng.2011.04.516.

[67] Park H, Kim S-J, Lee J, Kim JH, Kim D. Characterization of the Mechanical Properties of a High-Strength Laminated Vibration Damping Steel Sheet and Their Application to Formability Prediction. Met Mater Int 2019;25:1326–40.

[68] Bong HJ, Yoo D, Kim D, Kwon Y-N, Lee J. Correlative Study on Plastic Response and Formability of Ti-6Al-4V Sheets under Hot Forming Conditions. J Manuf Process 2020;58:775–86.

[69] Lee J, Bong HJ, Lee M-G. Return mapping with a line search method for integrating stress of the distortional hardening law with differential softening. Comput Struct 2021;257:106652. https://doi.org/https://doi.org/10.1016/j.compstruc.2021.106652.

[70] Park H, Kim S-J, Lee J, Kim JH, Kim D. Delamination behavior analysis of steel/polymer/steel high-strength laminated sheets in a V-die bending test. Int J Mech Sci 2020;173:105430. https://doi.org/10.1016/j.ijmecsci.2020.105430.

[71] Hershey A V. The plasticity of an isotropic aggregate of anisotropic face centred cubic crystals . J Appl Mech Trans ASME 1954;21:241-249.

[72] Hosford WF. A Generalized Isotropic Yield Criterion. J Appl Mech 1972;39:607–9.

[73] Sung JH, Kim JH, Wagoner RH. A plastic constitutive equation incorporating strain, strain-rate, and temperature. Int J Plast 2010;26:1746–71.

[74] Lee J, Kim JH, Lee MG, Barlat F, Zhou C, Chen Z, et al. Properties controlling the bend-assisted fracture of AHSS. Int J Plast 2015;75:100–20.

[75] Xue L, Wierzbicki T. Ductile fracture initiation and propagation modeling using damage plasticity theory. Eng Fract Mech 2008;75:3276–93.

[76] Davaze V, Vallino N, Feld-Payet S, Langrand B, Besson J. Plastic and fracture behavior of a dual phase steel sheet under quasi-static and dynamic loadings. Eng Fract Mech 2020;235:107165.

https://doi.org/https://doi.org/10.1016/j.engfracmech.2020.107165.

[77] Abaqus. User's Manual (2021). Hibbit,Karlsson & Sorensen Inc,.USA.; 2021.

[78] Sánchez PJ, Huespe AE, Oliver J. On some topics for the numerical simulation of ductile fracture. Int J Plast 2008;24:1008–38. https://doi.org/10.1016/j.ijplas.2007.08.004.

[79] Chalal H, Abed-Meraim F. Numerical Predictions of the Occurrence of Necking in Deep Drawing Processes. Metals (Basel) 2017;7:455. https://doi.org/10.3390/met7110455.

[80] Dunand M, Mohr D. Hybrid experimental – numerical analysis of basic ductile fracture experiments for sheet metals. Int J Solids Struct 2010;47:1130–43.

[81] Babuska TF, Pitenis AA, Jones MR, Nation BL, Sawyer WG, Argibay N. Temperature-Dependent Friction and Wear Behavior of PTFE and MoS2. Tribol Lett 2016;63:15. https://doi.org/10.1007/s11249-016-0702-y.

[82] NUMISHEET. NUMISHEET 2011 Benchmark. In: Chung K, Huh H, Han H-N, Moon YH, Barlat F, editors. 8th Int. Conf. Work. Numer. Simul. 3D Sheet Met. Form. Process., Seoul, Korea: 2011.

[83] Felipe Guzmán C, Saavedra Flores EI, Habraken AM. Damage characterization in a ferritic steel sheet: Experimental tests, parameter identification and numerical modeling. Int J Solids Struct 2018;155:109–22. https://doi.org/https://doi.org/10.1016/j.ijsolstr.2018.07.014.

[84] Zang SL, Guo C, Thuillier S, Lee MG. A model of one-surface cyclic plasticity and its application to springback prediction. Int J Mech Sci 2011;53:425–35. https://doi.org/10.1016/J.IJMECSCI.2011.03.005.

[85] Zang S, Lee M-G, Sun L, Kim JH. Measurement of the Bauschinger behavior of sheet metals by three-point bending springback test with pre-strained strips. Int J Plast 2014;59:84–107. https://doi.org/10.1016/J.IJPLAS.2014.03.015.

[86] Choi JH, Zang SL, Lee MG, Kim JH, Barlat F. Determining the coefficients of a

homogeneous anisotropic hardening model for ultrathin steel sheets. Int J Mech Sci 2019;157–158:428–38.

[87] Chen D, Li Y, Yang X, Jiang W, Guan L. Efficient parameters identification of a modified GTN model of ductile fracture using machine learning. Eng Fract Mech 2021;245:107535. https://doi.org/10.1016/j.engfracmech.2021.107535.

[88] Simo JC, Hughes TJR. Computational Inelasticity. Springer-Verlag; 1998.

[89] Lee J, Bong HJ, Kim D, Ha J. Modeling the multiaxial fracture behavior of Ti–6Al–4V alloy sheets at a high temperature using improved damage modeling. J Mater Res Technol 2023;25:1844–59. https://doi.org/https://doi.org/10.1016/j.jmrt.2023.06.059.

[90] Aravas N. On the Numerical Integration of a Class of Pressure-Dependent Plasticity Models. Int J Numer Methods Eng 1987;24:1395–416.

Declaration of interests

☒ The authors declare that they have no known competing financial interests or personal relationships that could have appeared to influence the work reported in this paper.

☐The authors declare the following financial interests/personal relationships which may be considered as potential competing interests: